Superconducting Coplanar Microwave Resonator

2022 CNF REU Intern: Sean C. Anderson, Jr.
Intern Affiliation: Electrical and Computer Engineering, Morgan State University

CNF REU Principal Investigator: Prof. Farhan Rana, Department of Electrical and Computer Engineering, Cornell University
CNF REU Mentor: Arjan Singh, Electrical and Computer Engineering, Cornell University

CNF REU Project and Primary Source(s) of Research Funding: 2022 Cornell NanoScale Science & Technology Facility Research Experiences for Undergraduates (CNF REU) Program via the National Science Foundation under Grant No. NNCI-2025233
Contact: seandl@morgan.edu, fr37@comell.edu, as2995@cornell.edu
Website: https://cnf.cornell.edu/education/reu/2022
Primary CNF Tools Used: AJA Sputter Deposition, ABM Contact Aligner, Hamatech Wafer Processor

Abstract:

We are trying to make on-chip superconducting microwave resonators which are capable of driving spins in semiconductors by using the superconducting metal niobium (Nb). These microwave resonators will work mainly in two ways; Sensing magnetic defects and magnetic order in thin films of new materials; Manipulating and measuring the quantum state of a collection of spin defects for use in quantum technologies. This will aid in the optimization of optics and optoelectronics. In the past, the Rana research group did a similar project with the coplanar microwave waveguide resonator, however, in that experiment, the smaller the dimensions of the metal of the deposited metal, which in that case was copper, then the smaller the extent the magnetic field will radiate outward and there will be greater conductive losses. This is the reason we chose to go with a superconductor, which minimizes conductive losses.

Summary of Research:

This summer research project focused on getting familiar with the cleanroom, learning about what a coplanar microwave resonator is, and aiding in the process of developing one that is superconducting.

The tools we used the most with this project were the AJA sputter deposition system to deposit niobium on a sapphire wafer, along with the ABM contact aligner for the UV exposure to the sapphire wafer, and then development with the Hematech development tool, which makes the pattern on the sapphire wafer visible using the 726 MlF solution for 60 seconds.

The working principles behind why the device will be resonant at certain frequencies has to do with the transmission lines on the device. A simple analogy can be made with the length of a string where its resonant frequency is directly related to its length by the equation f_o = velocity/ 2Length, which are considered standing waves.

The same is true of our transmission lines except that in AC electronics, we must consider the voltage and current waves and the rise and collapse of these waves, which will in turn give us a better idea of their resonant frequencies. The inductive and capacitive properties of the superconducting coplanar

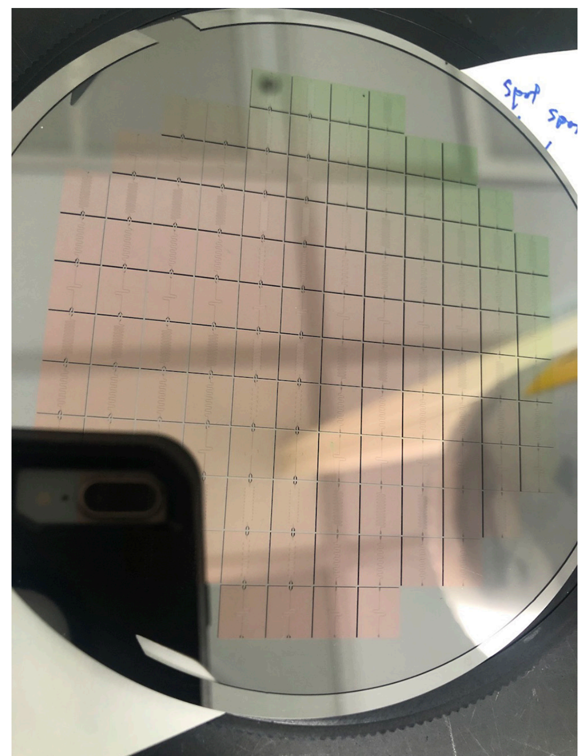

Figure 1: We designed three devices on the sapphire wafer.

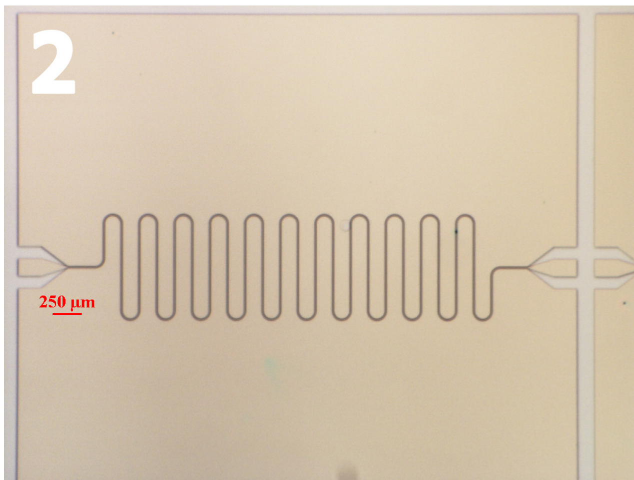

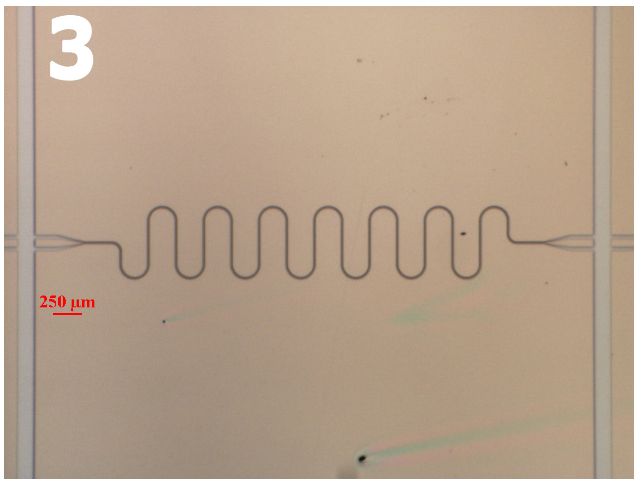

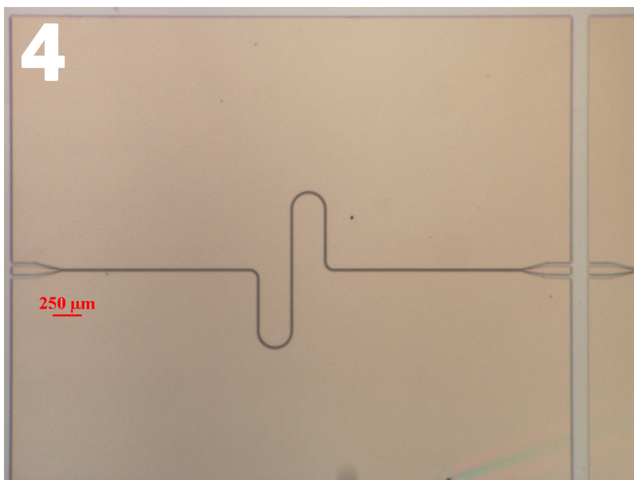

Figure 2-4: The respective resonant frequencies of each device are shown in an array on the sapphire wafer and are 2GHz at 29.62 mm (Figure 2 top), 4.l GHz at 14.61 mm (Figure 3 middle), and 8 GHz at 7.5 mm (Figure 4 bottom).

microwave resonator also gives rise to the resonant frequencies at which the device will operate. Given those two things, transmission line length and the reactive AC components of the device will determine the resonance at which the device operates.

We designed three devices on the sapphire wafer (Figure 1). The respective resonant frequencies of each device are shown in an array on the sapphire wafer and are 2GHz at 29.62 mm (Figure 2), 4.l GHz at 14.61 mm (Figure 3), and 8 GHz at 7.5 mm (Figure 4).

The idea was to sample materials using the superconducting coplanar microwave resonator, which entailed probing the resonator with a DC power source to get a static magnetic field that shoots out perpendicular to the coplanar microwave resonator's surface, and probing the device with a microwave frequency to be sent inside of the device, which created our oscillating magnetic field.

At microwave frequencies, the spin-states of the electrons will split into two even but opposite energies of El = +1/2gμBB and E2 = -1/2gμBB where ~ E = El - E2.

From there we could observe the electron's spin behaviors from the bode plot that was characterized from the material we sampled and which will be the future work to be performed on this device.

Conclusions and Future Steps:

The device is now ready for characterization, which means that we will next take a look at the transmission characteristics and see where our device is resonant at. Resonance will occur at microwave frequencies where $\hbar(\omega) = g\,\mu_B$.

References:

[1] Standing Waves and Resonance, Chapter 14 - Transmission Lines, Electronics Textbook (allaboutcircuits.com).

[2] Coplanar waveguide resonators for circuit quantum electrodynamics, Journal of Applied Physics 104, 113904 (2008); https://doi.org/10.1063/1.3010859; M. Göppl, A. Fragner, M. Baur, R. Bianchetti, S. Filipp, J. M. Fink, P. J. Leek, G. Puebla, L. Steffen, and A. Wallraff.

Microscale Broadband Optical Upconverter

CNF Project Number: 900-00

Principal Investigator(s): Paul L. McEuen[1,2,4]

User(s): Yanxin Ji[3], Alejandro J. Cortese[4], Conrad L. Smart[1]

Affiliation(s): 1. Laboratory of Atomic and Solid State Physics, Cornell University; 2. Kavli Institute at Cornell for Nanoscale Science, Cornell University; 3. Electrical and Computer Engineering, Cornell University; 4. OWiC Technologies

Primary Source(s) of Research Funding: Cornell Center for Materials Research (DMR1719875), Air Force Office of Scientific Research (MURI: FA9550-16-1-0031), New Frontier Grants from the Cornell College of Arts & Sciences, Cornell IGNITE Innovation Acceleration Program

Contact: plm23@cornell.edu, yj323@cornell.edu, cs2239@cornell.edu

Primary CNF Tools Used: Odd Hour Evaporator, ABM Contact Aligner, Oxford 81 Etcher, AJA Sputter Deposition Tool, Hot Press, Heidelberg Mask Writer DWL2000, Oxford Cobra ICP Etcher, PT770 Etcher

Abstract:

Optoelectrical materials/devices that convert long-wavelength light into shorter wavelengths have gained increasing interest in fields like bio-sensing and infrared imaging [1]. Here we present a microscale optical upconverter made by heterogeneously integrating Si photovoltaics (PVs) and GaN light emitting diodes (LEDs). Previous research on photon upconversion mainly focused on upconversion nanoparticles (by nonlinear anti-Stokes emission) [2]. This kind of upconversion is limited by the materials and has a narrow band of excitation/emission wavelength. In contrast, our optical upconverter can be excited by a wide range of light wavelengths: from visible to infrared light. The emission wavelength can reach blue or even shorter wavelengths which are determined by the LED's emission.

Summary of Research:

The broadband optical upconverter is made by fabricating silicon (Si) PVs and gallium nitride (GaN) LEDs separately and then integrating them together.

To fabricate Si PVs, we start from n-type doped SOI wafers and utilize phosphosilicate glass to dope the top layer, creating a vertical PN junction. The PVs' contacts and interconnect are Pt/Ti and are deposited through AJA sputtering tool. The PVs are isolated by inductively coupled plasma (ICP) etching (Cobra ICP etcher).

To fabricate GaN LEDs, we start from GaN heterostructure wafers (from a commercial vendor). The n-contacts and p-contacts are Au/Pd and Ti/Au respectively, which are deposited through e-beam evaporation. The LEDs are outlined by ICP dry etch via PT770 etcher.

After the PVs and LEDs are fabricated on their native substrates, we integrate them together through a transfer method developed by our group. We spin ~ 6 µm PMMA onto the LEDs as the protection layer. By using a thermoplastic polymer (polypropylene carbonate), we bond the LED substrate to a sapphire carrier wafer through Hot Press. Afterward, the LEDs' native substrate is removed by laser lift-off. In the end, the LEDs are aligned and transferred to the PV substrate via ABM contact aligner alignment and Hot Press bonding. The carrier wafer is removed through thermal slide. The polymer residue is cleaned in acetone.

Our upconverters are powered by long-wavelength light and emit short-wavelength light. The optical energy is firstly converted into electrical energy and then converted back to optical energy, which is an optical-electrical-optical (O-E-O) process. Si PVs carry out the optical-electrical conversion. Si's narrow bandgap (~1.1eV) enables a broad range of excitation photon energies. GaN LED performs the electrical-optical conversion. The efficiency of our upconverter is determined by the product of two efficiencies: Si PV's conversion efficiency (~20%) and GaN LED's light-emitting efficiency (~2%). Therefore, overall power efficiency can reach ~ 0.4%, which is comparable to the upconversion nanoparticles (~0.01%-1%) [3].

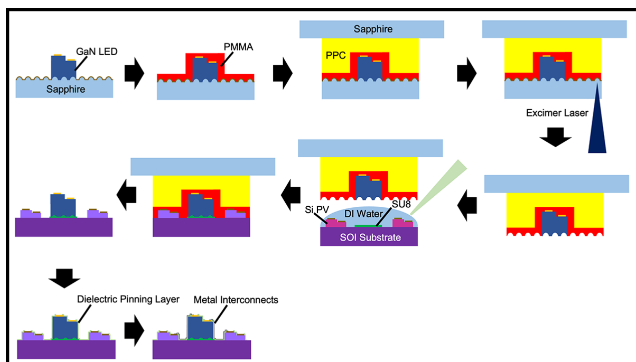

Figure 1: Schematic illustration of the upconverter integration process.

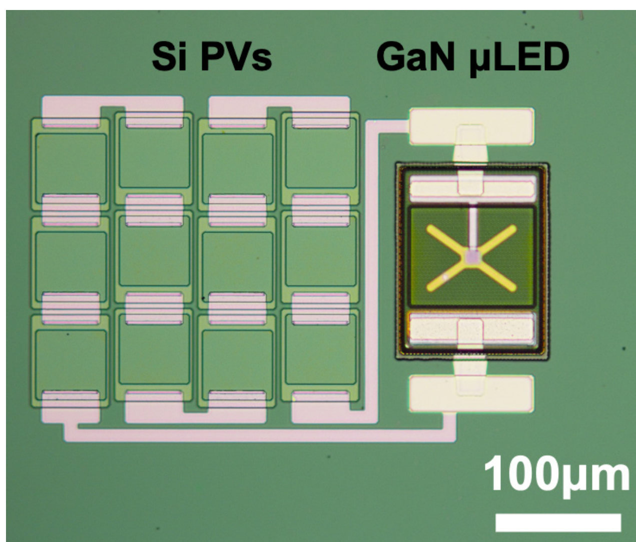

Figure 2: Optical image of an upconverter.

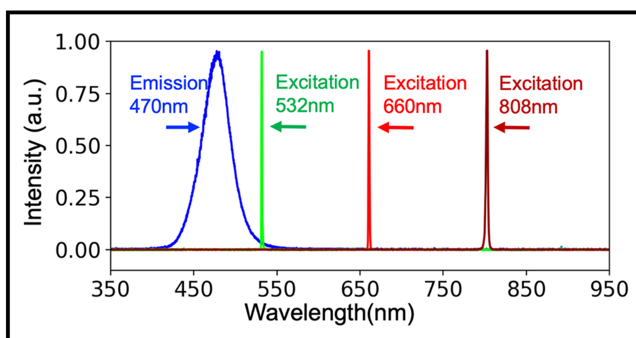

Figure 3: Spectra of the excitation source (532 nm, 660 nm, and 808 nm laser) and the upconverter's emission with a peak at 470 nm.

Conclusions and Future Steps:

Here we present a platform that enables microscale broadband optical upconverters made by heterogeneous integration of Si based PVs and III-V materials-based LEDs. This heterogeneous integration technique allows the fabrication of thousands of optical upconverters in parallel per wafer. The efficiency of the upconverter is ~ 0.4%, which is comparable to the best upconversion nanoparticles. Our next step is to make devices with more sophisticated functions based on this platform. It will be integrating CMOS circuits with III-V materials based optical devices.

References:

[1] Zhou, B., Shi, B., Jin, D. and Liu, X. Controlling upconversion nanocrystals for emerging applications. Nat. Nanotechnol. 10, 924-936 (2015).

[2] Auzel, F. Upconversion and anti-Stokes processes with f and d ions in solids. Chem. Rev. 104, 139-173 (2004).

[3] Algar, W. R. et al. Photoluminescent Nanoparticles for Chemical and Biological Analysis and Imaging. Chem. Rev. 121, 9243-9358 (2021).

Microscopic Optically Powered Bubble Rockets

CNF Project Number: 900-00

Principal Investigator(s): Paul L. McEuen

User(s): Samantha L. Norris, Michael F. Reynolds

Affiliation(s): Physics, Cornell University

Primary Source(s) of Research Funding: Cornell Center for Materials Research (DMR-1719875)

Contact: plm23@cornell.edu, sn588@cornell.edu, mfr74@cornell.edu

Primary CNF Tools Used: ABM Contact Aligner, Oxford Cobra/81/82/100 Etchers, Oxford ALD/PECVD, Heidelberg Mask Writer - DWL2000

Abstract:

Bubble propulsion as a swimming mechanism for artificial microswimmers has been of significant interest recently, especially for biomedical applications. We demonstrate hundred-micron-scale bubble-propelled microswimmers that produce bubbles via voltage-induced water electrolysis, allowing operation in any aqueous solution, including physiological saline. These bubble rockets are powered by onboard photodiodes, allowing individual addressability limited only by the power and divergence of the light beam. We also demonstrate the ability to design microswimmers with different trajectories based on device geometry, and show integration with thin-film magnets for *in situ* steering. Finally, we present a novel method for locomotion on a solid-liquid interface.

Summary of Research:

We present hundred-micron-scale bubble rockets that consist of onboard photodiodes used to convert incident light into a voltage and current for water electrolysis. A diagram of a microswimmer is shown in Figure 1a. Each device consists of multiple silicon P-N junctions wired in series with two platinum electrodes roughly shaped like a tapered hollow cylinder with a rectangular cross section. Each photodiode has an open-circuit voltage of roughly 0.65V with a responsivity of ~ 0.3 A/W under Hg lamp illumination and operates in a light intensity of 1 kW/m^2, roughly that of a sunny day. The entire device is encapsulated in silicon dioxide except for the interior of the hollow electrodes.

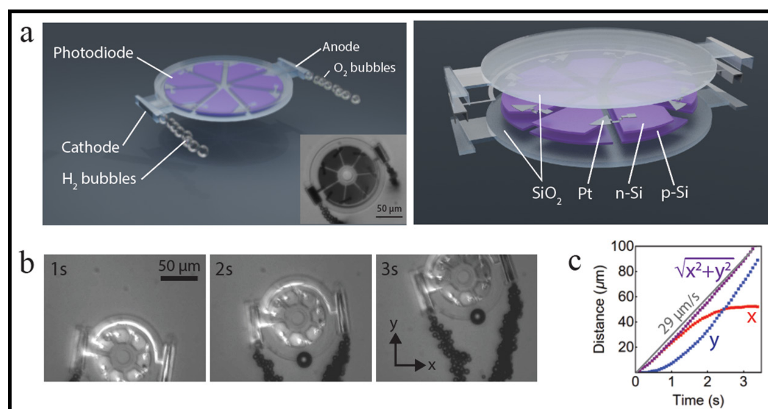

Figure 1: Diagrams and optical micrographs of optically powered microswimmer and time lapse of swimming behavior. a) Diagrams of optically powered microswimmer showing encapsulated photodiodes, hollow platinum electrodes, and bubble production. Inset: microswimmer operating on glass-water interface in 10 mM PBS solution under Hg lamp illumination. b) Time lapse of a device swimming under mercury lamp illumination at an air-water interface in 10 mM PBS solution. c) Displacement vs. time for the swimming device shown in b.

Under standard microscope illumination, the onboard photodiodes apply a voltage between the two electrodes sufficiently high to split water, producing hydrogen and oxygen gas at the cathode and anode respectively. The capillary force on these bubbles in the tapered cylinder forces them to be ejected from the tube, propelling the microswimmer forward.

A time lapse of a device swimming in 10 mM PBS is shown in Figure 1b, with a displacement vs. time curve in Figure 1c. This bubble rocket is swimming at roughly 30 µm/s at an air-water interface. Due to the stoichiometric ratio of hydrogen to oxygen produced during water splitting, the instantaneous velocity of the hydrogen-producing cathode is twice that of the oxygen-producing anode, resulting in a circular trajectory.

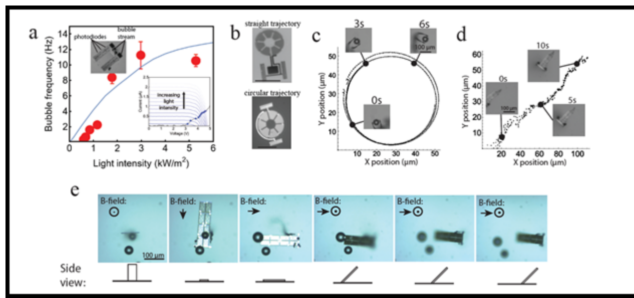

Figure 2: Description of microswimmer behavior. a) Measured bubble frequency as a function of incident light intensity for stationary microswimmer device (red) with expected bubble frequency from operating points in inset (blue). b) Micrographs of devices with circular and straight swimming trajectory showing wiring and electrode geometry. c) Time lapse and corresponding circular trajectory of a microswimmer with separate anodic and cathodic rockets on a solid-liquid interface. d) Time lapse and corresponding straight trajectory of a microswimmer with each rocket containing both anode and cathode on a liquid-liquid interface. e) Microswimmer on a solid-liquid interface with thin film magnets rotating in three dimensions and locomoting with an attack angle of 45 degrees to reduce friction.

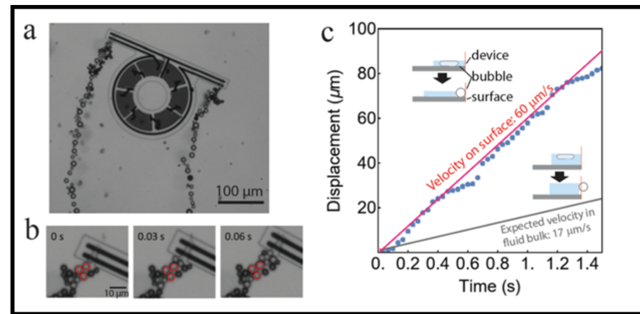

Figure 3: Utilizing bubble surface adhesion for increased surface swimming velocity. a) Micrograph of microswimmer locomoting on glass-water interface by pushing off ejected bubbles attached to the surface. b) Time lapse of microswimmer shown in (a) moving by approximately one bubble diameter with each bubble expulsion. c) Displacement as a function of time for device shown in (a) compared to maximum expected velocity using traditional bubble-propelled motion. Insets: diagrams showing mechanism of bubble propulsion for devices without (top) and with (bottom) a bottom on the rockets.

The relationship between bubble ejection frequency and incident light intensity can be understood by considering separately the current-voltage characteristics of the photodiodes and on-chip rocket-shaped electrodes. The bubble ejection frequency for a microswimmer is shown in Figure 2a; the frequency increases with input light intensity until the photodiodes become voltage limited. The I-V curves of the photodiodes and on-chip electrodes are shown in the inset.

In addition, we demonstrate the ability to control microswimmer trajectory both by controlling electrode geometry and by integrating onboard thin film magnets for steering in a uniform magnetic field. The current required for bubble nucleation on an electrode depends on the confinement of the produced gas. Although both anode and cathode of the microswimmer must be exposed to fluid for current to flow, the placement and geometry of the electrodes can be designed to allow different swimming trajectories, as shown in Figure 2b. Circular and linear trajectories are shown for microswimmers in Figure 2c-d. By fabricating Co magnets onboard the microswimmers and performing experiments in a three-axis solenoid, the microswimmers can also be rotated and steered in three dimensions as shown in Figure 2e.

We have also shown the ability to engineer the microswimmer/substrate interface for more effective locomotion on a flat surface, as shown in Figure 3. By removing the bottom of the tube-shaped electrode, bubbles are able to attach to the surface and remain stationary while the capillary force of bubble growth propels the microswimmer forward. As such, the swimmer moves forward roughly one bubble diameter with each bubble expulsion, leaving the bubbles behind as shown in Figure 3a. A time lapse of the rocket movement is shown in Figure 3b. Each rocket contains both anode and cathode, such that the overall device moves forward in a straight line, with its trajectory shown in Figure 3c.

In conclusion, we have demonstrated a truly microscale bubble-propelled swimmer that can swim in physiological solutions with a long lifetime, paving the way for intelligent bubble-propelled microrobots to be used in applications from drug delivery, to manipulation, to *in vivo* monitoring. These bubble rockets can be fabricated to swim with a circular or linear trajectory and can also be integrated with thin-film magnets for steering in a uniform magnetic field. Finally, we have shown a novel method for bubble-propelled locomotion on a solid-liquid interface.

Microwave-Rate Soliton Microcombs on a Monolithic $LiNbO_3$ Platform

CNF Project Number: 1997-11
Principal Investigator(s): Qiang Lin
User(s): Yang He, Mingxiao Li, Shixin Xue

Affiliation(s): Department of Electrical and Computer Engineering, University of Rochester
Primary Source(s) of Research Funding: Defense Threat Reduction Agency (HDTRA11810047)
Contact: qiang.lin@rochester.edu, yhe26@ur.rochester.edu,
mingxiao.li@rochester.edu, sxue4@ur.rochester.edu
Primary CNF Tools Used: JEOL JBX9500FS Electron-Beam Lithography System, AJA Ion Mill, SEM

Abstract:

We report microwave-rate soliton microcombs on a chip-scale lithium niobate platform.

Summary of Research:

Coherent microwaves play an important role in many applications, such as wireless communication, radar, imaging, and clocks. Among various approaches, soliton microcombs exhibit great potential for coherent microwave generation due to their good coherence properties in combination with chip-scale design. So far, radio-frequency-rate and microwave-rate soliton microcombs were produced only in silica and silicon nitride platforms [1-4]. Here we report microwave-rate soliton microcombs produced on a chip-scale lithium niobate platform, with repetition rate down to 13.5 GHz.

The devices are fabricated on the 610 nm Z-cut lithium niobate (LN) on insulator wafer. The etching thickness is about 420 nm and the waveguide width of the ring resonator is about 2.2 µm (Figure 1(a) insets). The group velocity dispersion is about -0.037 ps^2/m for the fundamental TE mode family, which is suitable for the soliton generation.

To tune the microwave frequency, we integrate an electro-optic modulator directly onto the comb resonator, as shown in Figure 1(a). Lithium niobate exhibits strong electro-optic Pockels effect, which is ideal for this purpose. For the z-cut comb resonator, we utilize the r_{31} EO term of lithium niobate to tune the quasi-TE comb modes of the resonator. The electrodes are deposited along the ring resonator waveguide with an electrode-waveguide spacing of about 4 µm so as to maintain the high optical Q of the resonator as well as good electro-optic tuning efficiency.

The repetition rate of the soliton microcombs, corresponding to the frequency of the microwave, is determined by the resonator size. By changing the radius of the ring resonator from 100 µm to 1500 µm, we are able to produce soliton microcombs with rep rate from 200 GHz to 13.5 GHz, as shown in Figure 1(b),(c),(d), and (g). As an example, Figure 1(d) and (g) show the spectra of the detected microwave at 19.8 and 13.5 GHz, respectively, which exhibit a signal-to-noise ratio of above 70 dB. The corresponding phase noise spectra are shown in Figure 1(f) and (i), respectively. For the 19.8 GHz signal (Figure 1(e)), the phase noise is about -40 dBc/Hz at 1 kHz, reaches -110 dBc/Hz at 10 kHz, and finally goes below -130 dBc/Hz at 3 MHz. The phase noise for the 13.5 GHz signal (Figure 1(h)) exhibits a similar phase noise level. The low phase noise indicates the high coherence of LN solitons, which is crucial for their applications in microwave photonics.

References:

[1] X. Yi, et al., "Soliton frequency comb at microwave rates in a high-Q silica microresonator," Optica 2, 1078 (2015).

[2] M. Suh and K. Vahala, "Gigahertz-repetition-rate soliton microcombs," Optica 5, 65 (2018).

[3] J. Liu, et al., "Photonic microwave generation in the X-and K-band using integrated soliton microcombs," Nature Photon. 14, 486 (2020).

[4] T. J. Kippenberg, et al., "Dissipative Kerr solitons in optical microresonators," Science 361, 567 (2018).

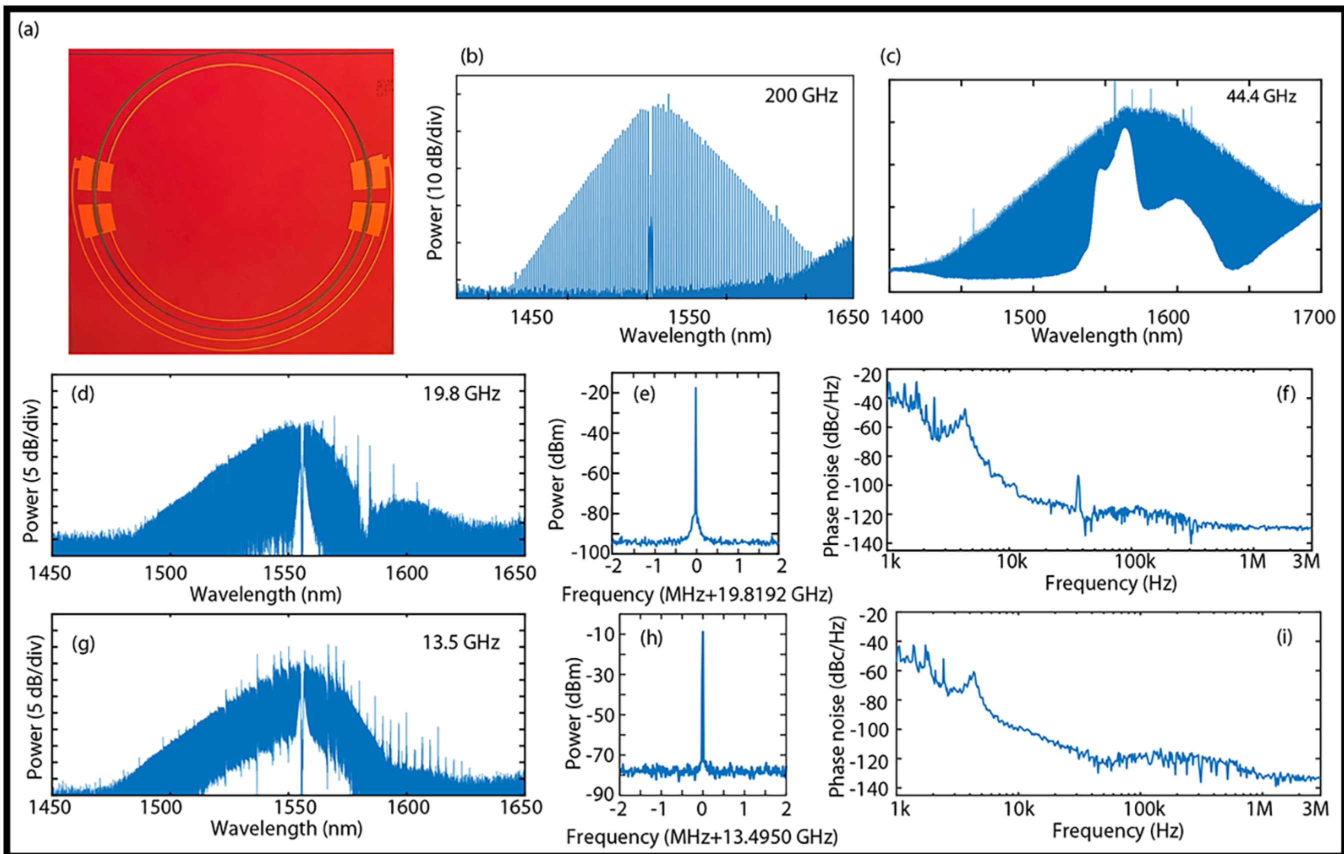

Figure 1: (a) Image of a ring resonator integrated with electrodes. Soliton spectra for LN ring resonators with radii of about 100 μm (b), 450 μm (c), 1020 μm (d), and 1500 μm (g). (e) ((h)) RF signal generated from soliton microcombs in (d) ((g)), and the RBW is 200 Hz. (f) ((i)) Measured phase noise of the RF signal in (e) ((h)).

Lithium Niobate Nanophotonic Resonators for Quantum Simulations

CNF Project Number: 1997-11

Principal Investigator(s): Qiang Lin[1,2]

User(s): Usman A. Javid[1]

Affiliation(s): 1. Institute of Optics, University of Rochester, Rochester NY.; 2. Department of Electrical and Computer Engineering, University of Rochester, Rochester NY.

Primary Source(s) of Research Funding: National Science Foundation (Grants No. EFMA-1641099, ECCS-1810169, and ECCS-1842691); Defense Threat Reduction Agency, Joint Scient and Technology Office for Chemical and Biological defense Grant No. HDTRA11810047; Defense Advanced Research Projects Agency (DARPA) Agreement No. HR00112090012

Contact: qiang.lin@rochester.edu, usman.javid@rochester.edu

Primary CNF Tools Used: JEOL 9500, AJA Ion Mill, SC4500 Evaporator

Abstract:

Integrated photonic devices have enabled momentous progress in development of scalable quantum computing and information processing technologies. These devices are designed to control quantum states of light confined within nanophotonic structures to implement computing protocols. To that end, we demonstrate a frequency domain analog quantum simulator that can simulate a two-dimensional lattice of atoms on the thin-film lithium niobate platform. The device is fabricated at the Cornell NanoScale Facility (CNF).

Summary of Research:

Quantum simulation is one of the primary computational tasks that a quantum computer can perform much more efficiently than a classical computer. Over the past two decades, significant efforts have been made for efficient simulation of condensed matter systems [1]. Integrated photonic devices are well-suited for these applications due to their inherent scalability that can help build large-scale simulation and perform computational tasks [2]. One of the most promising techniques for quantum simulation with light involves photons in distinct frequency modes. Here, we demonstrate frequency domain simulation of the tight-binding model. This model describes a chain of atoms that have nearest neighbor coupling. We implement this by coupling adjacent frequency modes of an optical resonator with electro-optic modulation done using on-chip electrodes. With this system, we demonstrate simulation of a two-dimensional quantum random walk and simulation Bloch oscillations of an electron in the presence of an eternal electric field.

The device used for these simulations is a nanophotonic racetrack resonator fabricated on 600-nm X-cut lithium niobate on insulator (LNOI) wafer. The ring has a width of 1.5 µm and an etch depth of 300 nm. The device is patterned on the wafer using electron-beam-lithography on the JEOL 9500 machine using ZEP520A as the resist mask. After development, the device is etched using argon ion milling on the AJA ion mill achieving a 50% (300 nm) etching depth. The resist is then stripped using standard resist remover chemistry and the chip is prepared for a second electron-beam exposure. This is to pattern electrodes on both sides of the resonator as previously stated. The material is coated with PMMA resist and exposed again to pattern the electrodes. After development, the chip is deposited with a 400 nm layer of gold using an evaporator (SC4500). The electrode pattern is subsequently created by a resist liftoff process in acetone. Figure 1 shows an optical microscope image of a fabricated device at different magnifications.

The simulations are run on the temporal evolution of entangled photon pairs inside the resonator. These photons are also generated within the resonator using spontaneous parametric down conversion (SPDC), a process in which a laser photon annihilates to generate a photon pair [3]. Figure 2 shows evolution of a quantum random walk of the photon pairs. Each pixel in the images represent a resonator mode pair. Photons in one mode of the resonator can scatter to its two adjacent modes using the on-chip electro-optic modulator driven at a microwave frequency matching the resonators mode spacing. This implements a coin toss experiment

OPTICS & OPTO-ELECTRONICS

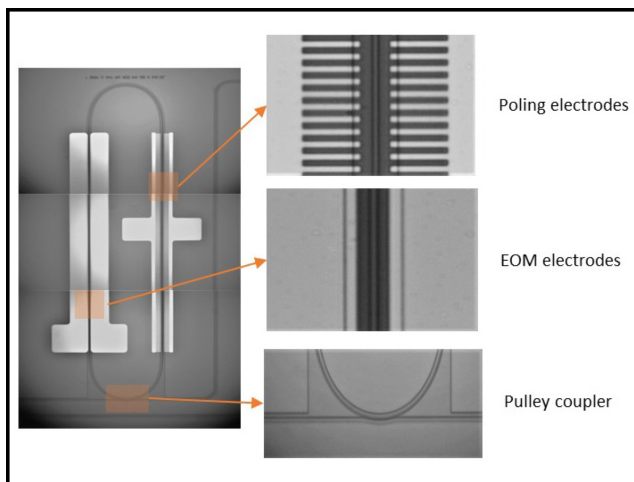

Figure 1: Microscope image of a fabricated device showing different sections of the device. These are: a ring resonator, an evanescently coupled waveguide to couple light into and out of the resonator, and electrodes patterned around the resonator.

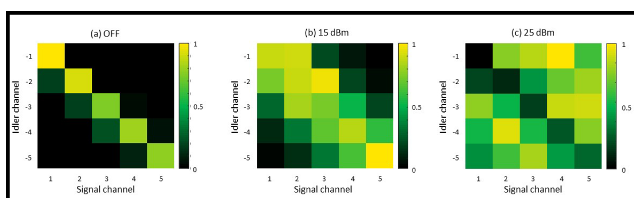

Figure 2: Quantum random walk of the frequency correlation of the photon pairs with (a) no modulation signal, (b) Microwave signal amplitude at 15 dBm and (c) at 25 dBm. The axes indicate the mode number of the resonator and the colormap shows the strength of the correlation at each mode pair. The spread of the correlation with increasing modulation amplitude is a signature of a random walk.

at each mode implementing the random walk. The spread of the random walk increases by increasing the mode coupling using a stronger microwave signal as shown in Figure 2. Another simulation we perform is motion of an electron under an influence of a constant electric field inside a crystal lattice. The electric field is simulated by detuning the microwave signal away from the resonator's mode spacing. This imparts a Bloch-like phase on the coupling [4]. Figure 3 shows the temporal correlation of the photon pairs. We see the correlation turns oscillatory when the microwave signal detuning is introduced with a frequency matching the detuning. These are Bloch oscillations simulated on the temporal correlation of the photon pairs.

Conclusions:

To conclude, we have designed and fabricated an optical quantum simulator based on thin-film lithium niobate. We have demonstrated simulation of quantum random walk and Bloch oscillations. Although these are simple simulations, they demonstrate the ability of this platform for frequency domain computational and simulation tasks. Furthermore, we envision that this demonstration will motivate experiments in quantum simulation on chip-scale architectures.

References:

[1] Reviews of Modern Physics 86.1 (2014): 153.

[2] Science 360.6386 (2018): 285-291.

[3] Reports on Progress in Physics 66.6 (2003): 1009.

[4] Optica 3.9 (2016): 1014-1018.

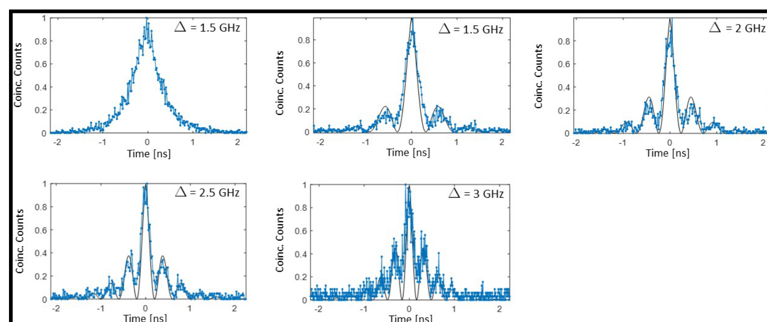

Figure 3: Temporal correlation of the photon pairs at different modulation detunings D. The oscillations occurring at non-zero detuning values are an analog of Bloch oscillations of an electron in the presence of a constant electric field.

Self-Injection-Locked Second-Harmonic Integrated Source

CNF Project Number: 1997-11

Principal Investigator(s): Qiang Lin[1,2]

User(s): Jingwei Ling[1], Jeremy Staffa[2]

Affiliation(s): 1. Department of Electrical and Computer Engineering, University of Rochester, Rochester NY.; 2. Institute of Optics, University of Rochester, Rochester NY

Primary Source(s) of Research Funding: Defense Advanced Research Projects Agency (DARPA) LUMOS program under Agreement No. HR001-20-2-0044, the Defense Threat Reduction Agency-Joint Science and Technology Office for Chemical and Biological Defense (grant No. HDTRA11810047), National Science Foundation (NSF) (ECCS-1810169, ECCS-1842691 and OMA-2138174)

Contact: qiang.lin@rochester.edu, jling8@ur.rochester.edu, jstaffa@ur.rochester.edu

Primary CNF Tools Used: JEOL 9500, AJA Ion Mill, CVC SC4500 Odd-Hour Evaporator, DISCO Dicing Saw

Abstract:

High coherence laser sources are centrally important to the operation of advanced position/navigation/timing systems [1] as well as classical/quantum sensing systems [2]. However, the complexity and size of these bench-top lasers impedes their transition beyond the laboratory. Here, a system on-a-chip that emits high-coherence visible and near-visible light is demonstrated. The devices use a new approach wherein wavelength conversion and coherence increase by self-injection-locking are combined within in a single nonlinear resonator.

Summary of Research:

Optical frequency conversion based upon a quadratic optical nonlinearity is a powerful technology to transfer high coherence laser radiation to new frequencies [3]. Recently, the development of nonlinear photonic integrated circuits (PICs), particularly the on-chip lithium niobate-on-insulator (LNOI) platform [4-8], have boosted nonlinear conversion efficiency while enabling photonic integration with active and passive waveguide elements. However, to achieve high coherence in these systems bench top source lasers have been used.

Here we demonstrate for the first time a hybridly-integrated laser that produces efficient and ultra-coherent near-visible light. The device combines second harmonic generation (SHG) in an LNOI microresonator that also functions to line narrow a DFB pumping laser through self-injection locking (SIL) [9].

The high-Q lithium niobate (LN) microresonator and distributed-feedback (DFB) diode laser are facet-to-facet coupled as shown in Figure 1a and b. The LN resonator provides both resonantly-enhanced SHG and feedback to line narrow the DFB pump. For SHG, it is periodically poled to quasi-phase match the resonant pump and up-converted modes. For line narrowing, the high-Q mode introduces weak backscattering into the DFB laser to achieve SIL. The pump coherence is readily transferred to the up-converted light, resulting in linewidth narrowing of the frequency-doubled light.

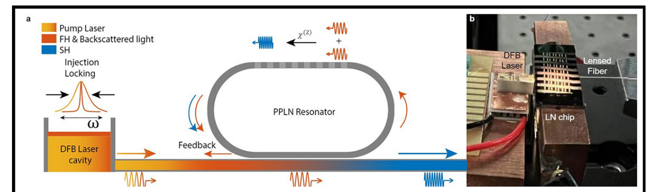

Figure 1: (a) Conceptual diagram of the self-injection locking and second-harmonic generation process. (b) Optical image of the self-injection-locked frequency-doubling chip system.

The race-track LN microresonator device is fabricated on congruent x-cut thin film lithium-niobate-on-insulator (LNOI), with 600 nm LN sitting upon a 4.7 µm silica layer. ZEP-520A resist is used for a first e-beam lithography step (JEOL 9500), followed by 300 nm Ar-ion milling (AJA ion mill) to define the devices. A second e-beam writing step is performed on PMMA resist, and 400 nm electrodes are created using a gold evaporation and lift-off process (CVC SC4500 odd-hour evaporator).

The poling process is similar to previously reported methods [6], but the poling is done after the etching process. The poling uniformity can be observed in Figure 2b. We target SHG of a 1560 nm pump to a near-infrared wavelength near 780 nm.

Maximum conversion occurs at the pump wavelength of 1559.5 nm. By fixing the laser wavelength at this

resonance the SHG output power versus coupled power is measured in Figure 3.

Maximum SHG power is 11.3 mW at a pump power of 44.6 mW, corresponding to a conversion efficiency of about 25%. This conversion efficiency is among the highest reported to date for on-chip LN devices [4,5,7,8]. The measurements are in good agreement with the theory (solid curves), which predicts a maximum conversion efficiency of 28%.

The frequency noise of the self-injection locked pump laser is characterized with a self-heterodyne approach [10] while the noise of SHG light is measured with a conventional homodyne detection setup with quadrature-point locking [11]. The results are shown in Figure 4. The high-offset-frequency pump noise is significantly reduced compared to the free-running DFB laser by over 20 dB, demonstrating the effect of the SIL process. The SHG noise reaches a level of 1600 $Hz^2\ Hz^{-1}$ at around 3 MHz offset frequency. These data place the SHG short-term linewidth in the range of 10-30 kHz. Because the SHG frequency noise is fundamentally proportional to the square of the doubled pump noise, the SHG frequency noise must therefore be 4× larger (6 dB) than the pump frequency noise.

Conclusions and Future Steps:

We have demonstrated a highly-efficient, chip-scale laser that produces high-coherence light by combining SIL and SHG within a single high-*Q* nonlinear resonator. A SH linewidth as narrow as 10 kHz is achieved by suppression of pump frequency noise. On-chip converted power over 2 mW is obtained in a hybrid-integrated design. An external pump laser yields a maximum conversion efficiency over 25% and maximum SHG power of 11.3 mW. These measurements suggest much higher integrated device performance will be possible by replacing this hybrid design with a heterogeneously-integrated device that features low pump to LN resonator coupling loss. This approach can be applied to other optical frequency conversion processes such as optical parametric oscillation for frequency down-conversion, and third-harmonic generation. Moreover, the on-chip LN platform enables integration with electro-optic components for further functional enhancement.

Acknowledgements:

Thank you to Heming Wang, Boqiang Shen, Lue Wu, Zhiquan Yuan, and Bohan Li from Professor Kerry J. Vahala's group Caltech and to Lin Chang from John E. Bower's group at UCSB for their essential collaborative work on this project, as well as to Usman A. Javid, Raymond Lopez-Rios, Mingxiao Li, and Yang He from Qiang Lin's group.

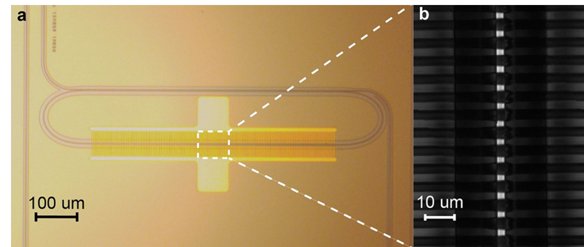

Figure 2: (a) Optical image of the PPLN racetrack resonator. Dashed box gives region of grating imaged in panel b. (b) 2nd-harmonic confocal microscope image of the periodically poled waveguide section showing the uniformity of periodic poling.

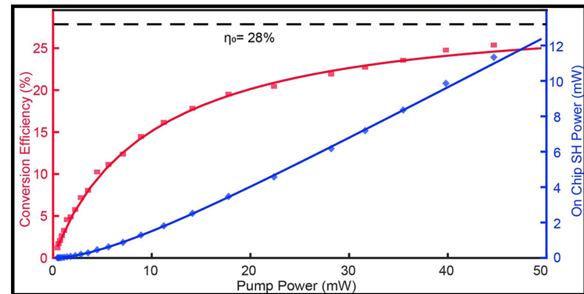

Figure 3: SHG power (blue diamonds) and conversion efficiency (red squares) as a function of the pump power on chip.

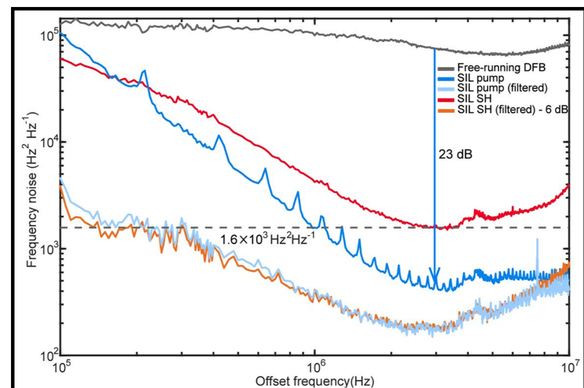

Figure 4: Recorded frequency noise spectrum. Grey, blue and red traces show the frequency noise spectrum of the free-running DFB laser, SIL pump laser, and SIL frequency-doubled light, respectively. The light blue trace and the orange traces show the frequency noise of the pump light and 6 dB down-shifted SHG light when frequency jumping noise is removed from data.

References:

[1] 2014 ISISS, 1-4 (IEEE, 2014).
[2] Reviews of modern physics 89, 035002 (2017).
[3] Physics today 47, 25-33 (1994).
[4] Optica 5, 1438-1441 (2018).
[5] Optica 6, 1455-1460 (2019).
[6] Optics Express 28, 19669-19682 (2020).
[7] arXiv:2102.05617 (2021).
[8] Laser & Photonics Reviews 15, 2100091 (2021).
[9] Optics letters 12, 876-878 (1987).
[10] Journal of Lightwave Technology 26, 30483055 (2008).
[11] Nature Photonics 6, 369-373 (2012).
[12] https://arxiv.org/abs/2207.03071.

Two-Dimensional TMD as a Single Photon Source and a Quantum Sensor

CNF Project Number: 2126-12

Principal Investigator(s): Gregory Fuchs, David Muller

User(s): Jaehong Choi

Affiliation(s): Applied and Engineering Physics, Cornell University

Primary Source(s) of Research Funding: Air Force Office of Scientific Research Multidisciplinary Research Program of the University Research Initiative (AFOSR MURI)

Contact: gdf9@cornell.edu, jc3452@cornell.edu

Primary CNF Tools Used: JEOL 6300, Oxford COBRA, 5X g-line Stepper, Wire Bonder, DISCO Dicing Saw, SC4500 Odd-Hour Evaporator, AFM – Veeco Icon, Zeiss Supra SEM, Zeiss Ultra SEM

Abstract:

Electronic and optical properties of two-dimensional transition metal dichalcogenides (2D TMDs) are readily tuned by strain and external fields due to their atomic thickness. Tensile strain is known to confine excitons and create single photon emitters in 2D TMDs. We are working toward using electron microscopy to directly measure the strain to better understand the strain confinement of excitons. Also, the exciton emission energy in TMDs can be tuned with an external field and we tried using an interlayer exciton in homobilayer tungsten diselenide (WSe_2) as a quantum sensor for the polarization change in ferroelectric materials in vicinity.

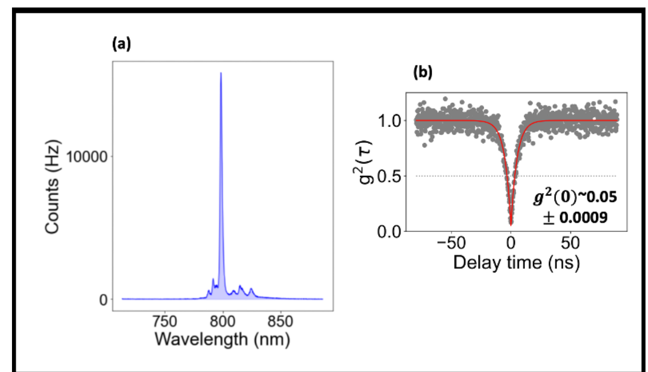

Figure 1: (a) Spectrum from the fold at the nanogap site. We observed an emission peak with a narrow linewidth, which implies a strong exciton confinement. (b) Time correlation measurement of the emitter created at the nanogap. We observed the antibunching with $g^2(0)$ value ~ 0.05, which unambiguously shows the high purity of the single photon emitter.

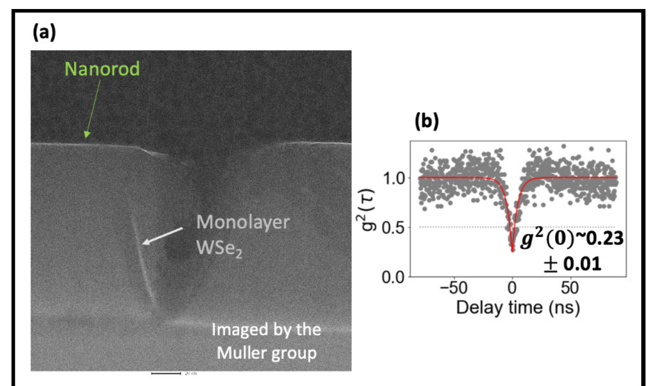

Figure 2: (a) TEM image of a nanogap site with the sharply folded monolayer WSe_2. (b) Time correlation measurement of a quantum emitter created at the sharp fold in (a). $g^2(0)$ is 0.23, which shows a single photon nature of the emitter.

Summary of Research:

Single photon emitters with high brightness and purity are key components for quantum communication and information technologies. Monolayer transition metal dichalcogenides (TMDs) have been established as promising sources of single photon emitters, and a recent study showed that the hybridization of strain-localized excitonic state and localized defect state induces single photon emission in monolayer WSe_2 [1]. To better understand the interplay among strain, exciton, and defect, it is crucial to have a clear picture of strain localization of excitons.

Electron microscopy is promising for the direct measurement and quantification of strain responsible for single photon emission in monolayer WSe_2. We were able to create single photon emitters by stacking monolayer WSe_2 on top of a nanorod-gap array. Monolayer WSe_2 is folded into nanogaps (90 nm) between nanorods, and the high strain point at the wrinkle confines excitons to create single photon emitters with high purity (Fig.1).

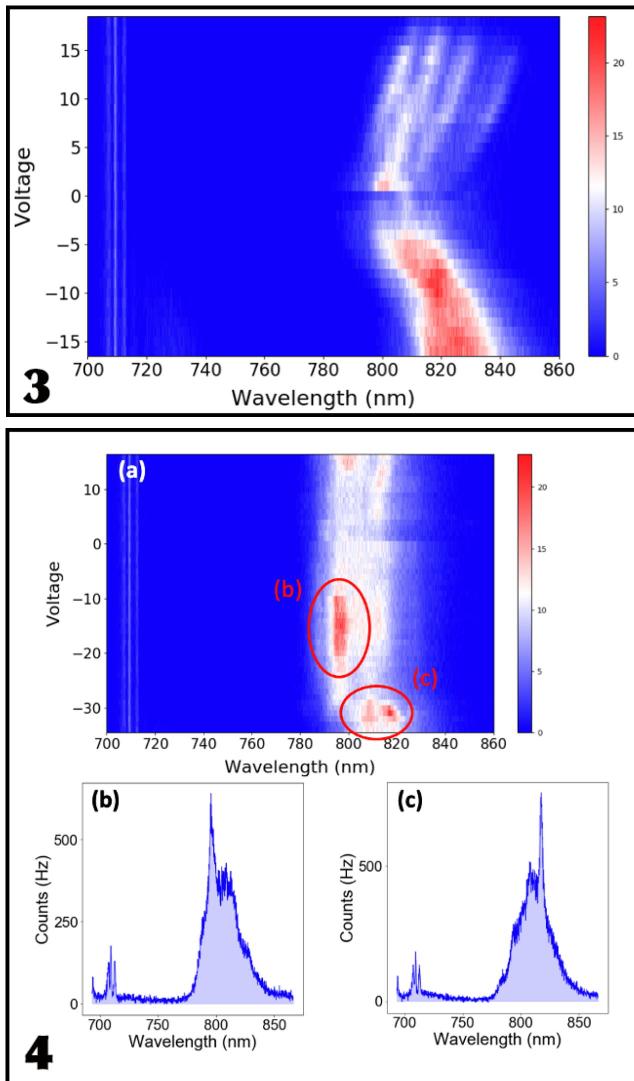

Figure 3, top: Photoluminescence modulated by V_{gb}. V_{tg} is adjacent to 2L-WSe_2, and it directly pumps charge carriers into 2L-WSe. We can see a clear doping effect. Figure 4, bottom: (a) Photoluminescence modulated by V_{tg}. V_{tg} is adjacent to BTO, and it switches the polarization in BTO. (b) and (c) show the change in population proportion of $\Lambda - K$ and $\Lambda - \Gamma$ indirect excitons under the polarization switching in BTO.

To better understand the strain confinement of excitons at the wrinkle apex, Transmission electron microscopy (TEM) imaging was attempted on the nanogap sites in collaboration with the Muller group at Cornell University. By TEM imaging, we confirmed that the high strain achieves a strong confinement of a single exciton. Anti-bunched quantum emitters were observed at sharp folds (Figure 2). At relatively flat and gradual folds, the strain was expected to be small. This resulted in creation of multiple emitters.

One of the pre-requisites for the strain analysis is that the atom columns in the material should be aligned with the beam axis. However, monolayer WSe_2 is thin and flimsy. We were unable to align the beam axis with the atom columns in WSe_2. To allow the strain analysis, it is important to have a support layer that gives a structural support so that the curvature of wrinkle is uniform throughout a monolayer WSe_2.

The next step is using a thick support layer underneath monolayer WSe_2 which will enable the strain analysis.

2D TMDs can be used as quantum sensors as well due to their sensitivity to their immediate environment. In homobilayer (2L) WSe_2, the Bloch states of valleys at each point in the momentum space have different orbital compositions, and this makes wavefunctions reside at different positions in real space and form interlayer exciton (2). Due to the spatial distance between an electron and a hole, interlayer excitons possess a dipole moment in an out-of-plane direction. This dipole moment can be modulated by an external field (2-4), so an interlayer exciton can be used to sense a polarization-induced field in ferroelectric materials in vicinity (4,5).

We studied the optical property change in 2L-WSe_2 in response to the polarization change in ferroelectric BTO in 2L-WSe_2/BTO hybrid heterostructure. A gate voltage was applied to modulate the polarization in BTO *in situ*. We observed that the spectral change in response to the polarization switching. When the bottom gate (V_{bg}), which is adjacent to 2L-WSe, was modulated, we observed a clear doping effect (Figure 3). When we modulated the top gate (V_{tg}), which is adjacent to BTO, the population proportion of indirect $\Lambda - K$ and $\Lambda - \Gamma$ excitons was changed at different voltage values (Figure 4). We wanted to see the hysteresis, but BTO started leaking at higher voltages, so the higher range voltage sweep was not possible. Next step is using a much thicker BTO membrane to minimize the leaking and study the photoluminescence change in WSe_2 when the polarization switches in BTO.

Conclusions and Future Steps:

Deterministic activation of single photon emitters is crucial for quantum technology application, and a better understanding of exciton confinement that leads to single photon emission is required. Electron microscopy on the strained monolayer WSe_2 will enable us to directly measure and quantify the strain responsible for single photon emission. Homobilayer WSe_2 was used to sense the polarization change in ferroelectric BTO. Interlayer exciton emission energy and spectral composition are expected to be modulated by the polarization-induced field in ferroelectric BTO. Thick BTO will be used to minimize the leaking and allow a wide range of voltage sweep.

References:

[1] Linhart, L., et al, Phy. Rev. Lett. 123, 146401 (2019).

[2] Huang, Z., et al, Phy. Rev. Lett. B 105, L041409 (2022).

[3] Altaiary, M., et al, Nano Lett. 22, 5, 1829-1835 (2022).

[4] Wang, Z., et al, Nano Lett. 18, 1, 137-143 (2018).

[5] Li, T., et al., Nano Lett. 17, 922.927 (2017).

[6] Li, P., et al., Adv. Funct. Mater. 2201359 (2022).

Sputtered Oxide Integrated Photonics

CNF Project Number: 2297-14
Principal Investigator(s): Amy Foster
User(s): Neil MacFarlane, David Irvine, Aaron Schreyer-Miller

Affiliation(s): Electrical and Computer Engineering Department, Johns Hopkins University

Primary Source(s) of Research Funding: Viavi Solutions, Inc.
Contact: amy.foster@jhu.edu, nmacfar2@jhu.edu, dirvine4@jhu.edu, aschrey1@jh.edu
Primary CNF Tools Used: Oxford 100 Etcher, Oxford PECVD, PT770 Etcher, Zeiss SEM, JEOL 6300

Abstract:

Niobium tantalum dioxide (NbTaOx) is a material developed by collaborator Viavi Solutions. NbTaOx films are deposited using low temperature pulsed DC magnetron sputtering. We have been investigating NbTaOx as a new platform for both linear and nonlinear integrated photonics. We have fabricated ring resonators with quality factors as high as 858,000 corresponding to propagation losses as low as 0.47 dB/cm. Using these high-quality ring resonators, we have also investigated the nonlinear capabilities of the NbTaOx platform and demonstrated optical parametric oscillation.

Summary of Research:

NbTaOx is a high linear refractive index material, with a linear refractive index that is about 10% higher than that of silicon nitride at a wavelength of 1550 nm. This high refractive index results in a high index contrast with respect to the typical silicon dioxide (SiO_2) cladding material. The higher contrast produces highly confined waveguide modes, allows for tighter waveguide bending radii, and enhanced nonlinear interactions.

Our waveguides were dispersion engineered for broadband nonlinear interactions, which require anomalous dispersion. Through design and simulation, it was found that the required film thickness for anomalous waveguide dispersion at C-band wavelengths was about 800 nm. Because these films are deposited using a sputtering deposition technique, depositing 800 nm thick films does not come with the same challenges associated with depositing thick Si_3N_4 films like stress induced film cracking. The waveguide devices were patterned using electron-beam lithography. We used a chromium etch mask was dry etched using the CNF PT770 etcher. The NbTaOx film was then etched using the CNF Oxford 100 etcher. The devices were clad with SiO_2 and diced into individual chips. SEM images of waveguide cross section and side wall are shown in Figure 1.

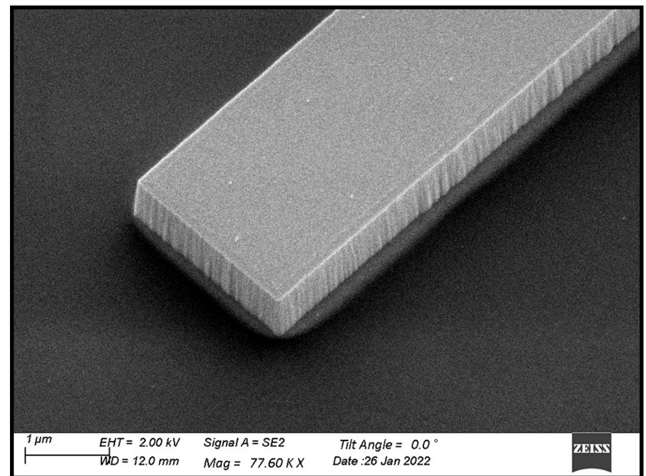

Figure 1: SEM image of NbTaOx waveguide sidewall.

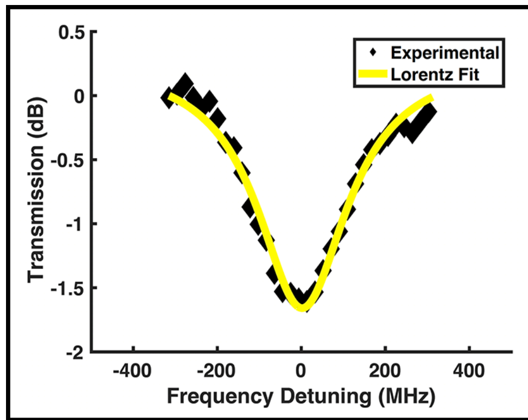

Figure 2: Individual resonance fit to a Lorentzian function.

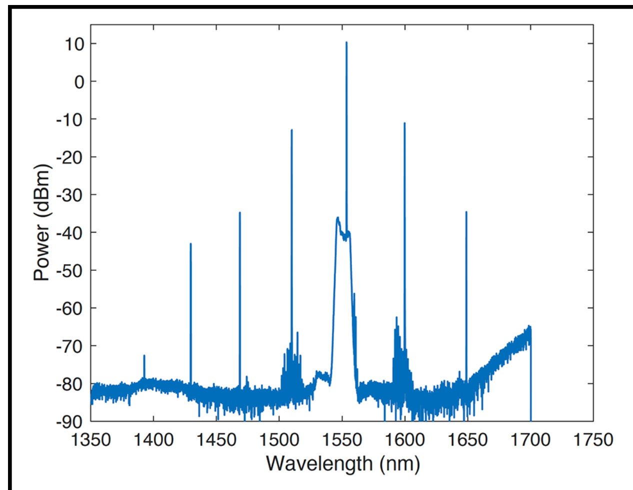

Figure 3: a) Spectrum of optical parametric oscillator generated in NbTaOx ring resonator.

The linear transmission of the waveguides was measured as a function of propagation length ranging from 0.6 cm to 2.8 cm. The losses varied from 0.56 dB/cm to 0.99 dB/cm for waveguide widths of 3.5, 2.5, and 1.5 µm.

We also extracted propagation losses by measuring the spectrum of high-quality ring resonators. The resonator spectrum for the 2.5 µm waveguide width are shown in Figure 2. The highest quality factor resonance was found to be 858,000, which corresponds to linear propagation losses of 0.47 dB/cm.

Using the high-quality ring resonator, we investigated the nonlinear capabilities of the NbTaOx films by generating optical parametric oscillation. The spectrum of the frequency comb is shown in Figure 3. We couple a high-power pump on-chip and slowly tune its wavelength to one of the resonance wavelengths of the device. Once the round-trip optical parametric gain via four-wave mixing within the ring exceeds the round-trip losses, the four-wave mixing process spontaneously generates single and idler sidebands of an optical parametric oscillator shown in Figure 3.

Conclusions and Future Work:

Our initial investigation into the NbTaOx films indicated that they are a high-quality platform for both linear and nonlinear integrated photonics. These results are the first demonstration of frequency comb generation in this material platform. Some of our immediate future work is to lower the oscillation threshold and to fill in more comb lines of the Kerr frequency comb. This will be done through a combination of fabrication optimization as well as decreasing the size of the ring resonators. In addition to this, we plan to investigate the minimum bending radius capabilities of this platform and use this information to demonstrate dense and complex linear integrated photonic circuits.

Development of Single and Double Layer Anti-Reflective Coatings for Astronomical Instruments

CNF Project Number: 2458-16

Principal Investigator(s): Gordon Stacey[1]

User(s): Bugao Zou[2]

Affiliation(s): 1. Department of Astronomy,
2. Department of Applied and Engineering Physics, Cornell University

Primary Source(s) of Research Funding: NASA Grant NNX16AC72G

Contact: stacey@cornell.edu, bz332@cornell.edu

Primary CNF Tools Used: Oxford Plasma Enhanced Chemical Vapor Deposition, Anatech Resist Strip, Oxford 81/82/100 Etchers, Manual Resist Spinners, Resist Hot Strip Bath, Plasma-Therm Deep Silicon Etcher, ASML 300C DUV Stepper, JEOL JBX 9500FS Electron-Beam Lithography System

Abstract:

The Epoch of Reionization Spectrometer (EoR-Spec) is one of the instrument modules to be installed in the Prime-Cam receiver of the Fred Young Submillimeter Telescope (FYST). This six-meter aperture telescope will be built on Cerro Chajnantor in the Atacama Desert in Chile. EoR-Spec is designed to probe early star-forming regions by measuring the [CII] fine-structure lines between redshift z = 3.5 and z = 8 using the line intensity mapping technique. The module is equipped with a scanning Fabry-Perot interferometer (FPI) to achieve the spectral resolving power of about RP = 100. The FPI consists of two parallel and identical, highly reflective mirrors, forming a resonating cavity called etalon. The mirrors are silicon-based and patterned with double-layer metamaterial anti-reflection coatings (ARC) on one side and metal mesh reflectors on the other. The double-layer ARCs ensure a low reflectance at one substrate surface and help tailor the reflectance profile over the FPI bandwidth. Here we present the design and fabrication processes of silicon mirrors for the FPI.

Summary of Research:

The goal of the project is to develop microfabricated, silicon-substrate-based mirrors for use in cryogenic Fabry-Perot Interferometers for astronomical instruments in the mid-infrared to sub-mm/mm wavelength regimes. The mirrors consist of high-purity, float-zone, 500-µm-thick silicon wafers that are lithographically patterned with frequency-selective, gold mesh reflectors. Due to the high index of refraction of silicon, the other side of the mirror must be patterned with an ARC to achieve the broadband capability and mitigate contaminating resonances from the silicon surface [1,2].

The deep reactive-ion etching (DRIE) technique was employed to etch bulk silicon. It involves the Bosch processes which use alternate SF_6 and C_4F_8 gas exposures to produce near-vertical sidewalls and high aspect ratio features [3]. The fabrication recipe of the double-layer ARC structure is outlined in Figure 1.

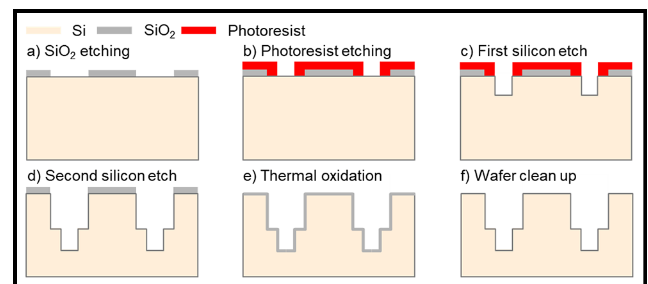

Figure 1: Key fabrication processes of the double-layer ARC structure.

Before performing DRIE silicon etches, we patterned SiO_2 and photoresist grids as two silicon etch masks, defining the upper and lower geometry. Process (a) comprises three individual steps.

The SiO_2 layer was first deposited onto the wafer by an Oxford plasma-enhanced chemical vapor deposition (PECVD) machine. Another layer of UV photoresist was then printed above the SiO_2 using an ASML PAS 5500/300C DUV Wafer Stepper with a resolution of 0.2 µm, serving as the oxide etch mask. A final oxide etch in an Oxford inductively coupled plasma (ICP) dielectric etcher with O_2 and CHF_3 gases transferred the grid pattern from the photoresist to the SiO_2 layer. The photoresist residue was removed further in an O_2 asher. The other photoresist silicon etch mask was then spun and exposed by the same stepper mentioned before, shown in process (b).

After a short descum and seasoning process, we proceeded to do the first silicon etch using a Plasma-Therm DRIE deep silicon etcher. When the target depth was reached, the wafer was cleaned with an O_2 plasma for half an hour at 3000 W to remove the photoresist and C_4F_8 related passivation residue. Then the second silicon etch was carried out, which constructed the upper ARC layer and pushed the lower ARC layer further down to the designated depths.

To further improve the morphology of the etched surfaces, we adopted a thermal oxidation and a clean-up process. We grew a sacrificial layer of thermal SiO_2 of about 1.1 µm thickness using water vapors at 1200°C for 100 mins in a furnace and then removed it by a hydrofluoric acid (HF) bath. The growth of the thermal SiO_2 layer and undercuts caused by previous etching processes widened the hole structure on both layers. Therefore, we shrank the dimensions on the mask designs by 1 to 2 µm accordingly to compensate for it. A scanning electron microscope (SEM) images of the double-layer ARC structure are shown in Figure 2.

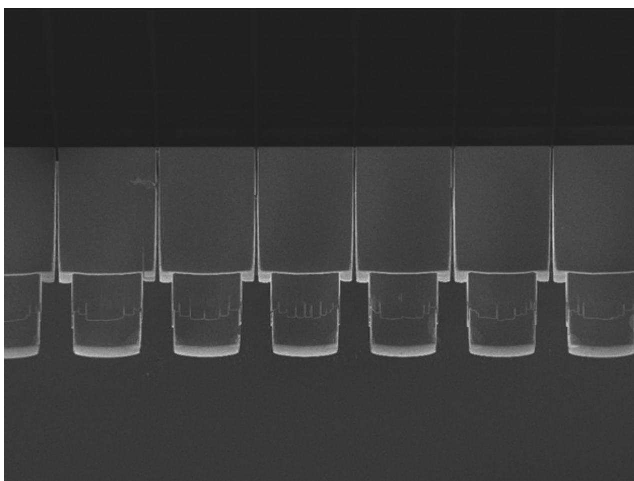

Figure 2: An SEM image showing the two-layer structure of anti-reflection coatings.

After constructing the double-layer ARC structure on one side of the silicon wafer, a layer of 2 µm photoresist was spun and baked on top of it to protect it from scratches and dust. Standard electron beam lithography, metal evaporation, and lift-off technologies were used to pattern the metal mesh structure on the other side. We coated the standard electron beam resist PMMA on the wafer and exposed it in a JEOL JBX 9500FS electron-beam lithography system with a maximum resolution of 6 nm. The wafer was then descumed and mounted inside a CVC SC4500 e-gun evaporation system where a 10 nm chromium adhesion layer and a 100 nm gold layer were evaporated. Afterward, we soaked the wafer into a Microposit 1165 remover bath heated to 80°C to lift the gold-coated PMMA layer off.

Conclusions and Future Steps:

In the past year, we have refined our past recipes with electron-beam lithography to achieve better resolution. We have demonstrated our ability to fabricate double-layer ARCs for different wavelengths and metal meshes with different feature sizes. We also published a new paper [4] about the design and characterization of the silicon mirrors in SPIE.

Our next steps are to better characterize our etched geometries and improve our metamaterial ARCs using Fourier transform spectrometers, and then use the results to iterate on our fabrication design.

References:

[1] Cothard, N., Choi, S., Duell, C., et al. The Design of the CCAT-prime Epoch of Reionization Spectrometer Instrument. J Low Temp Phys (2020). https://doi.org/10.1007/s10909-019-02297-1.

[2] N.F. Cothard, M. Abe, T. Nikola, G.J. Stacey, G. Cortes-Medellin, P.A. Gallardo, B.J. Koopman, M.D. Niemack, S.C. Parshley, E.M. Vavagiakis, K. Vetter, "Optimizing the efficiency of Fabry-Perot interferometers with silicon-substrate mirrors," Advances in Optical and Mechanical Technologies for Telescopes and Instrumentation III (2018).

[3] Chattopadhyay G, Reck T, Lee C, et al. Micromachined packaging for terahertz systems [J]. Proceedings of the IEEE, 2017, 105(6): 1139-1150.

[4] Zou B, Choi S K, Cothard N F, et al. CCAT-prime: The Design and Characterization of the Silicon Mirrors for the Fabry-Perot Interferometer in the Epoch of Reionization Spectrometer [J]. arXiv preprint arXiv:2207.08318, 2022.

Fabrication Strategy for Large-Area Meta-Optic Elements Exceeding the Exposure Size Limits of Lithography Tools

CNF Project Number: 2471-16

Principal Investigator(s): Professor Federico Capasso

User(s): Joon-Suh Park

Affiliation(s): John A. Paulson School of Engineering and Applied Sciences, Harvard University

Primary Source(s) of Research Funding: Defense Advanced Research Projects Agency (Grant no. HR00111810001)
Contact: capasso@seas.harvard.edu, parkj@g.harvard.edu
Website: https://www.seas.harvard.edu/capasso
Primary CNF Tools Used: Heidelberg Mask Writer - DWL2000, HamaTech Mask Chrome Etch 1, ASML 300C DUV Stepper, Gamma Automatic Coat-Develop Tool, CHA Mark 50 E-beam Evaporator, Plasma-Therm Dual Chamber 770, Oxford 81, Oxford 82, Oxford 100, P10 Profilometer, Disco Dicing Saw, Zeiss Ultra SEM

Abstract:

We show a fabrication path for creating a mass-producible metalens that works at visible wavelength, exceeding the inherent exposure size limit of the currently available lithography tools. We use the rotational symmetry of the metalens to save the number of required photomasks (reticles) for cost-efficiency, and therefore create a 10 cm diameter metalens from seven reticles with 2 cm × 2 cm exposure areas at wafer-scale, respectively.

Summary of Research:

For imaging at low-light conditions, one needs to increase the imaging optic's diameter to take in more light. However, simply increasing the diameter of an imaging lens faces two important tradeoffs in their application: the increase in aberration and the weight of the optic itself.

For applications in aerial drones or satellite imaging systems, where the payload is one of the primary concerns, simply increasing the lens diameter is therefore not a desirable option.

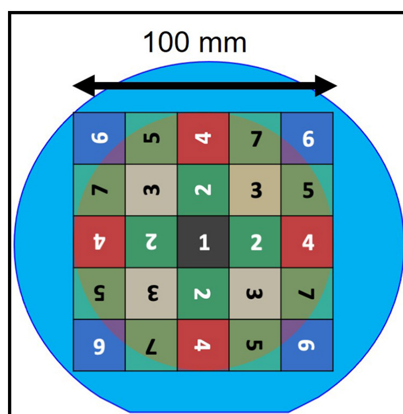

Figure 1: 10 cm diameter metalens fabrication strategy: The metalens is divided into 25 sections of 20 mm × 20 mm area, respectively. Only seven reticles are needed to expose the whole metalens by exploiting the rotational symmetry of the metalens.

Here, we show our process development in creating a 10 cm diameter, ultrathin metasurface lens (metalens) consisting of 18.7 billion nano-structures with DUV projection lithography, which is more than 40 times thinner and 16.5 times lighter than a refractive lens with similar optical power.

A metasurface optical element consists of sub-wavelength spaced structures on a two-dimensional surface that alters the incoming light and produce a designed outgoing wavefront. Each subwavelength structure in the metasurface locally change the transmitted light's amplitude, phase, polarization, or wavenumber in a way that one can design the combined wavefront to create optical functions, such as metasurface lenses (metalenses) [1], orbital angular momentum beam generators [2], polarization-dependent holograms [3], or Jones-matrix holograms [4].

For a metasurface optical element to function at a visible wavelength, the constituent sub-wavelength structures are required be in the order of few tens to hundreds of nanometers to avoid efficiency losses by high-order diffraction. Fabrication of such a metasurface therefore requires high-resolution lithography process such as electron-beam lithography or DUV lithography to be able to resolve such features. In the recent years, we have shown that a mass-production of metalenses with 1 cm in diameter and diffraction-limited performing at visible wavelength is possible with DUV lithography [5].

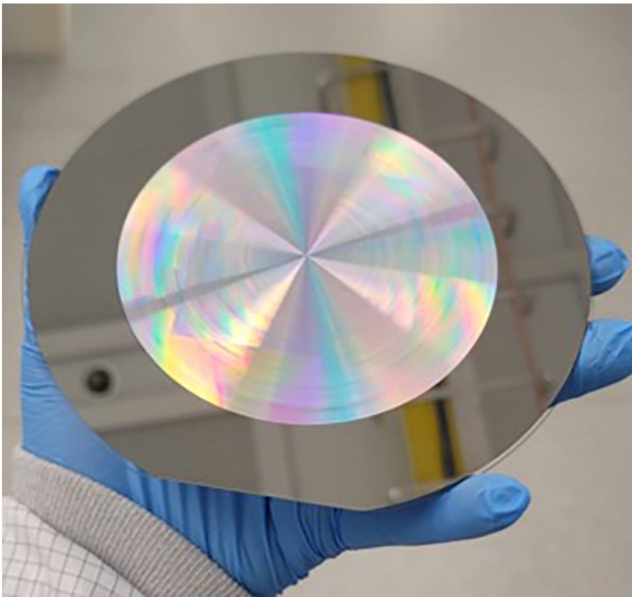

Figure 2: Photograph of the 10 cm diameter metalens' photoresist pattern on an aluminum coated 150 mm fused silica wafer.

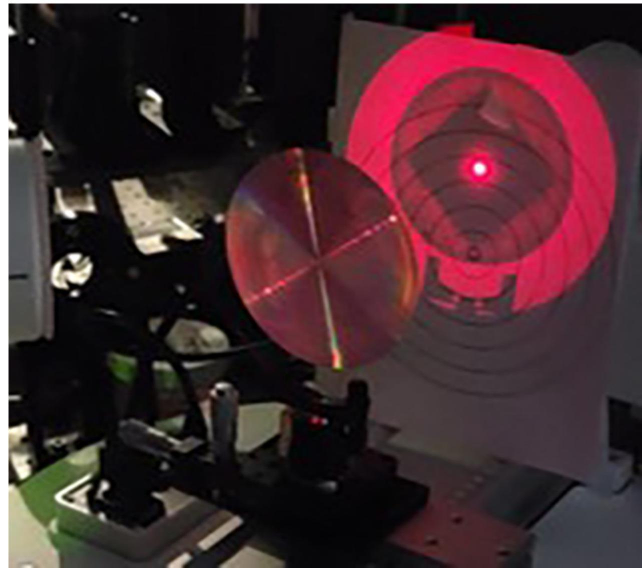

Figure 3: Photograph of the 10 cm diameter metalens focusing collimated He-Ne laser (633 nm).

To create a 10 cm diameter metalens, however, one faces size limitations restricted by the fabrication methods. With the conventional stepper lithography tools having maximum exposure area of 32 mm × 22 mm on a wafer per die, the stepper restricts the maximum diameter of a circular aperture metalens to 22 mm. To overcome such limitations, we divide the metalens into 25 sections, each consisting of 20 mm × 20 mm area.

For cost-effective fabrication, we use the rotation symmetry of the metalens to reduce the number of required reticles (Figure 1). As the metalens is rotationally symmetric, we can expose the whole 10 cm metalens with only seven reticles, instead of 25, if we rotate the wafer 90, 180, 270 degrees to expose each section, respectively, with global alignment process that has alignment error less than an order of magnitude smaller than the metalens' target wavelength. Figure 2 shows the result of DUV (248 nm, KrF) projection lithography of 10 cm diameter metalens on an aluminum coated 150 mm fused silica wafer. DUV lithography was performed with DUV-24P ARC layer and UVN2300 negative DUV resist.

Figure 3 shows the fabricated 10 cm diameter, all-glass metalens, focusing a collimated visible (λ = 633 nm) beam. The reticles for the central section (sections 1, 2, and 3 in Figure 1) were fabricated by an industry-grade photomask company, and outer sections 4-7 were fabricated with CNF tools (Heidelberg Mask Writer - DWL2000). As the reticles are of different quality, one can see the diffraction efficiency difference between the fields visible in the transmitted collimated beam at the focal plane of the metalens. Such difference can be resolved if all reticles are fabricated from the same source.

As the whole lens is fabricated with CMOS foundry compatible process, the shown metalens is mass-producible by IC chip companies. Detailed results and analysis are being prepared for peer-reviewed publication.

Conclusions and Future Steps:

We demonstrated a proof-of-concept fabrication of mass-manufacturable, all-glass 10 cm diameter metalens, capable of focusing monochromatic visible wavelength. We are further investigating on finding a path toward a broadband, achromatic, and large diameter metalens.

References:

[1] M. Khorasaninejad, W.T. Chen, R.C. Devlin, J. Oh, A.Y. Zhu, and F. Capasso, "Metalenses at visible wavelengths: Diffraction-limited focusing and subwavelength resolution imaging," Science 352, 1190 (2016).

[2] H. Sroor, Y.-W. Huang, B. Sephton, D. Naidoo, A. Valles, V. Ginis, C.-W. Qiu, A. Ambrosio, F. Capasso, and A. Forbes, "High-purity orbital angular momentum states from a visible metasurface laser," Nature Photonics 14, pp. 498-503 (2020).

[3] J. P. Balthasar Mueller, N.A. Rubin, R.C. Devlin, B. Groever, and F. Capasso, "Metasurface Polarization Optics: Independent Phase Control of Arbitrary Orthogonal States of Polarization," Physical Review Letters 118, 11, pp. 113901 (2017).

[4] N.A. Rubin, A. Zaidi, A.H. Dorrah, Z. Shi, and F. Capasso, "Jones matrix holography with metasurfaces." Science Advances 7, 33, eabg7488 (2021).

[5] J.-S. Park, S. Zhang, A. She, W.T. Chen, P. Lin, K.M.A. Yousef, J.-X. Cheng, and F. Capasso, "All-Glass, Large Metalens at Visible Wavelength Using Deep-Ultraviolet Projection Lithography," Nano Letters 19, 12, 8673-8682 (2019).

Prototype Photolithography for Multilayer Diffractive Lenses

CNF Project Number: 2472-16

Principal Investigator(s): Gennady Shvets

User(s): Giovanni Sartorello

Affiliation(s): School of Applied and Engineering Physics, Cornell University

Primary Source(s) of Research Funding: National Cancer Institute (award number R21 CA251052), National Institute of General Medical Sciences (award number R21 GM138947) of the National Institutes of Health

Contact: gs656@cornell.edu, gs664@cornell.edu

Primary CNF Tools Used: Heidelberg Mask Writer - DWL2000, SÜSS MicroTec Gamma Cluster Tool, ASML PAS 5500/300C DUV Stepper, Oxford PlasmaLab 100 ICP Etcher

Abstract:

We test a photolithography process to be used to fabricate large scale multilevel diffractive optics for use in thin optical systems.

Summary of Research:

Conventional optical systems, based on refractive lenses, must be of a certain thickness to perform their function. Optical requirements sometimes make such system impractically large and heavy. Solutions for some applications have included Fresnel lenses and gradient-index optics, and newer and intensively studied approaches include negative-index metamaterials, resonator-based metalenses and multilevel diffractive optics. The latter are ultrathin (few-wavelength) optical elements that use diffraction of radially symmetric elements, rings of various heights, to bend light. They can have the same imaging performance as metalenses while not being much thicker, and being faster and cheaper to fabricate [1]. Multilevel optics can be fabricated by repeated photolithography and etching steps with a sequence of patterns on the same wafer, whose superposition produces the final multilevel structure. After N steps, the MLD device has 2^N levels [2].

As a proof of concept, single-level samples to explore this process were fabricated at CNF on a silica wafer using the ASML DUV stepper with masks made with the Heidelberg Mask Writer - DWL2000. Each sample is about 1.5 mm across and contains circular features ranging from several dozen micrometers down to less than a micrometer. The wafer was coated in antireflective coating (ARC) and UV210 resist, exposed, processed

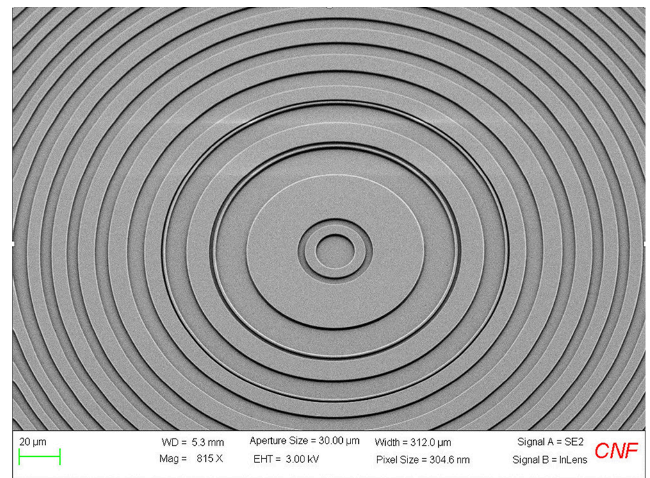

Figure 1: 35° SEM view of the center of one of the fabricated structures.

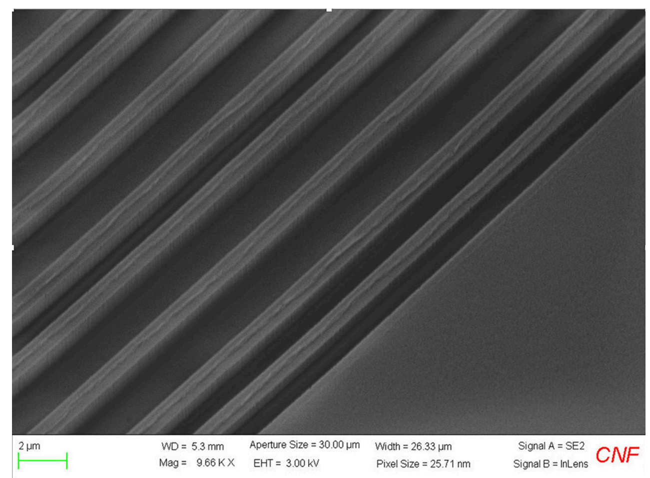

Figure 2: 35° SEM view of the edge of one of the fabricated structures.

in the Gamma tool and, after ARC removal, etched in the Oxford 100 etcher with a slow, consistent etching recipe. The resulting samples have well-defined edges both near the center, where features are largest (Figure 1), and near the edges, where they are finest (Figure 2), although the smallest (sub-micron) features are shallower than the design. By using a photolithographic process, the individual samples can be large (eventually, only limited by wafer size) and dozens can be made on a single wafer with little increase in overall fabrication time.

Conclusions and Future Steps:

The process has been proven suitable for the first step in the fabrication of a MLD system. Future tests would involve the fabrication of the remaining levels by repeating the process for 2-7 steps with a different exposed pattern each, using markers for alignment between layers. Tweaking the resist type and deposition method will be necessary to prevent pooling as the levels become deeper, and the etching method must be refined to achieve uniform depth even for the smallest features.

References:

[1] Banerji, S., Meem, M., Majumder, A., Vasquez, F. G., Sensale-Rodriguez, B., and Menon, R. (2019). Imaging with flat optics: metalenses or diffractive lenses? Optica, 6(6), 805. https://doi.org/10.1364/optica.6.000805.

[2] Saha, S. C., Li, C., Ma, Y., Grant, J. P., and Cumming, D. R. S. (2013). Fabrication of Multilevel Silicon Diffractive Lens at Terahertz Frequency. IEEE Transactions on Terahertz Science and Technology, 3(4), 479-485. https://doi.org/10.1109/TTHZ.2013.2251929.

Integrated Optical Gyroscope with Inverse Weak Value Amplification

CNF Project Number: 2524-17
Principal Investigator(s): Jaime Cardenas
User(s): Meiting Song

Affiliation(s): The Institute of Optics, University of Rochester

Primary Source(s) of Research Funding: Leonardo DRS
Center for Emerging and Innovative Science (CEIS)

Contact: jaime.cardenas@rochester.edu, msong17@ur.rochester.edu
Website: https://www.hajim.rochester.edu/optics/cardenas/

Primary CNF Tools Used: ASML Stepper, Oxford 100 Etcher, Oxford PECVD, LPCVD Nitride, DISCO Dicing Saw, XeF_2 Etcher

Abstract:

Weak value amplification has been demonstrated to enhance interferometric signals. We apply inverse weak value amplification to an integrated Sagnac interferometer gyroscope and demonstrate rotation measurement with the weak value gyroscope.

Summary of Research:

Gyroscopes are key elements for systems such as motion sensing and navigation. Optical gyroscopes using Sagnac effect are being widely adopted for their high sensitivity and reliability. Recently, micro optical resonators have been used for integrated optical gyroscopes [1,2], which are compact and robust for field applications. However, Sagnac phase scales with size and quality factor of the ring. Due to the small area and shorter lifetime in the cavity, micro ring resonator gyroscopes are generally less sensitive than optical fiber gyroscopes. Therefore, we apply integrated weak value amplification device to a Sagnac interferometer with ring resonator to increase its signal-to-noise ratio and sensitivity without increasing the size of the ring. This combined weak value gyroscope paves the way for more applications of integrated gyroscopes in fields that require high sensitivity and stability.

Weak value amplification can enhance interferometric signal-to-noise ratio [3], which optical gyroscopes rely on to increase sensitivity. Weak value amplification is a technique that takes a small amount of the dataset in a slightly perturbed system to enhance the signal without increasing the noise floor. For example, in the dark port of a balanced interferometer, ideally there is no light output. However, by introducing a small phase front tilt to the beam, a light beam appears at the dark port and the path-dependent phase shifts can be converted to location shift of the beam. This beam location shift, determined by a location-sensitive detector, yields to

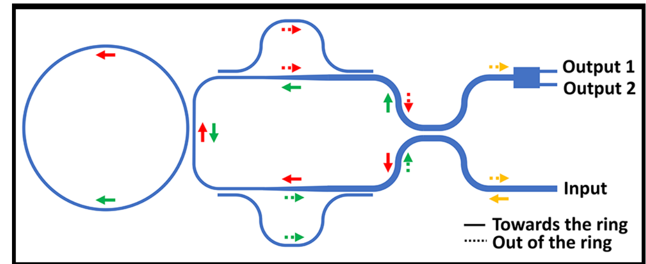

Figure 1: Schematic of integrated gyroscope with inverse weak value amplification (not to scale).

a larger signal than a traditional interferometer. In the meantime, it does not add additional noise compared to the traditional interferometers. Therefore, it can also be applied to optical gyroscopes, whose main component is Sagnac interferometer.

We use our integrated weak value device to detect interferometric signals from a ring resonator to measure rotation as a gyroscope. In a regular Sagnac interferometer, rotation is transferred to a phase difference between the clockwise and counterclockwise propagating light. In our weak value gyroscope, we use integrated weak value device to determine the phase difference between the two paths. The light is sent in through the bright port of the weak value device and gets split into two paths (Figure 1). The two paths

OPTICS & OPTO-ELECTRONICS

couple to the ring resonator in different directions and accumulate Sagnac. Then they become the two inputs of the weak value device. They both go through a phase front tilter and interfere at the multimode directional coupler. The final beam location shift can also be interpreted as a phase front tilt. Therefore, at the dark port of the interferometer, we use a MMI (multimode interferometer) to determine the amount of phase front tilt of the light, which contains the information of rotation-dependent phase shift.

The device is fabricated with silicon nitride platform and CMOS compatible processes. We deposit 300 nm thick silicon nitride on 4 µm of silicon dioxide and pattern the interferometer. Then we etch the silicon nitride layer and deposit another layer of 2 µm silicon dioxide on top with PECVD (plasma enhanced chemical vapor deposition). All waveguides are patterned with DUV photolithography and etched by ICP-RIE (inductively coupled plasma reactive ion etching).

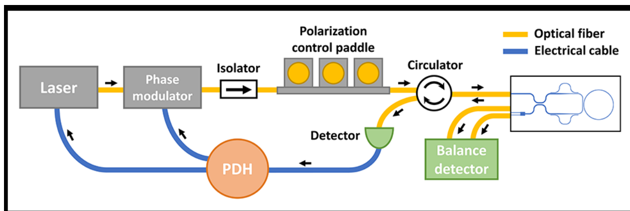

Figure 2: Testing setup of weak value gyroscope with PDH laser stabilization.

To characterize the performance of our weak value gyroscope, we mount the chip onto a motorized rotation stage and measure its angular velocity (Figure 2). We fuse a ribbon fiber with CO_2 laser to couple light around 1550 nm wavelength in and out of the device [4]. The light from the two dark port waveguides is sent to a balanced detector to get the power difference between them. The bright port is sent to a PDH system to lock the laser frequency to the resonance of the ring. The rotation phase in the bright port is in the TE1 mode and it is filtered out with a waveguide taper. We rotate the gyroscope back and forth in 1-sec steps while monitoring the balanced detector reading.

The gyroscope signal increases with rotation speed. The signal is calculated over 20 steps. Each step is averaged over 0.8 sec to avoid acceleration and deceleration. The gyroscope signal follows the rotation pattern of 1-sec rectangle waves as shown in Figure 3. The averaged signal shows linear relationship to the rotation rate up to 8°/sec (Figure 4). The loss of linearity could be due to the laser stabilization running out of tunability for long time operation. It can be improved by optimizing the PDH system settings.

Conclusions and Future Steps:

Integration of weak value amplification device with gyroscope can increase its sensitivity and enjoy the advantage of compactness and low noise. By adding weak value technique into micro ring gyroscopes, the sensitivity could be brought up one magnitude higher, which makes it more practical for field applications. The sensitivity can be improved with better quality factor of the ring resonator.

References:

[1] Y.-H. Lai, M.-G. Suh, Y.-K. Lu, B. Shen, Q.-F. Yang, H. Wang, J. Li, S. H. Lee, K. Y. Yang, and K. Vahala, "Earth rotation measured by a chip-scale ring laser gyroscope," Nature Photonics 14, 345-349 (2020).

[2] W. Liang, V. S. Ilchenko, A. A. Savchenkov, E. Dale, D. Eliyahu, A. B. Matsko, and L. Maleki, "Resonant microphotonic gyroscope," Optica, OPTICA 4, 114-117 (2017).

[3] M. Song, J. Steinmetz, Y. Zhang, J. Nauriyal, K. Lyons, A. N. Jordan, and J. Cardenas, "Enhanced on-chip phase measurement by inverse weak value amplification," Nat Commun 12, 6247 (2021).

[4] J. Nauriyal, M. Song, R. Yu, and J. Cardenas, "Fiber-to-chip fusion splicing for low-loss photonic packaging," Optica, OPTICA 6, 549-552 (2019).

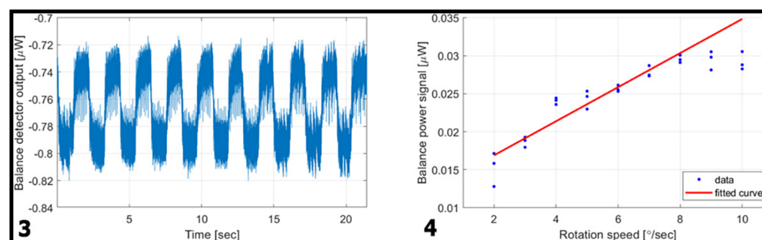

Figure 3, left: Balanced detector output of 5°/sec rotation, 1 sec time step. Figure 4, right: Weak value gyroscope signal vs. rotation speed.

Monolithic Multispectral Color Filter Array

CNF Project Number: 2524-17
Principal Investigator(s): Jaime Cardenas
User(s): Jiewei Xiang

Affiliation(s): The Institute of Optics, University of Rochester

Primary Source(s) of Research Funding: National Science Foundation
Contact: jaime.cardenas@rochester.edu, jxiang6@ur.rochester.edu
Website: https://www.hajim.rochester.edu/optics/cardenas/
Primary CNF Tools Used: ASML Stepper, Oxford 100 ICP-RIE, YES EcoClean Asher, Oxford PECVD, Furnace, JEOL 9500, Heidelberg Mask Writer - DWL2000, ABM Contact Aligner, Oxford Cobra ICP Etcher, Woollam RC2 Spectroscopic Ellipsometer, Oxford ALD FlexAL, Logitech Orbis CMP, AJA Sputter System

Abstract:

We introduce subwavelength grating and selective suppression to a Fabry-Perot cavity. We demonstrate a miniaturized monolithic broadband multispectral color filter with more than 40% transmission and less 30 nm full width at half maximum (FWHM).

Summary of Research:

A CMOS compatible multispectral color filter array with miniatured size is desired for the application in displays, image sensors and multispectral imaging. Many conventional multispectral imaging systems consist of a dispersive element (prism or grating) to separate the wavelengths, which makes the system challenging to further miniaturize [1]. Many transmissive color filters based on surface plasmon resonance and dielectric metasurfaces have been demonstrated to have high spatial resolution and small pixels. However, due to large FWHM (>50nm), low transmission (<40%) and high angular sensitivity, it is challenging to apply them to multispectral imaging.

People propose to combine multiple thin-film color filters based on Fabry-Perot (FP) resonators for high-quality MSFA [2]. Compared to a color filter based on diffraction, an FP resonator is polarization insensitive and relatively angular insensitive. It also has a high transmission and a narrow FWHM. The transmission peaks are tuned by changing the thickness of the cavity with lithography and etching. Due to the increasing steps of fabrication, it is challenging to have many detection channels. To overcome this challenge, people propose to introduce a 2D subwavelength grating structure inside the resonance cavity to manipulate the optical path length and control the transmission peak [3]. However, due to the properties of FP resonators, there will be multiple resonance peaks which constrain the free spectral range (FSR). Also, due to the limitation of fabrication, the fill ratio of the subwavelength grating structure cannot be too high which would result in a small spectral tuning range.

We demonstrate a broadband multispectral FP color filter array based on two-dimensional subwavelength gratings and selective suppression [4], which can cover from red to near-infrared (630nm-960nm) with narrow bandwidths (<30nm). Our thin-film color filter stack consists of two DBR mirrors and a cavity with two layers of subwavelength gratings sandwiching a thin metal layer (Figure 1). To achieve a large tuning range, we apply a combination of mesh and grating structures (Figure 2) and use the second-order resonance of the FP resonator with selective suppression. We change the effective index of the cavity to tune the location of the transmission peak. Instead of using the first-order transmission peak, we choose the second-order transmission peak for its smaller reflection phase. Also, the second-order transmission peak has a narrower linewidth compared to the first-order transmission peak due to a larger optical path length in the cavity, which makes the FWHM of our filters smaller than 30 nm. By inserting a metal layer in the middle of the cavity, the odd-order transmission peaks will be largely suppressed, which allows the second-order resonance to have a comparable FSR with the first-order resonance.

There are mainly six steps for the fabrication of our color filter array (Figure 1). We use polysilicon as the high index material for both DBR and cavity. Polysilicon

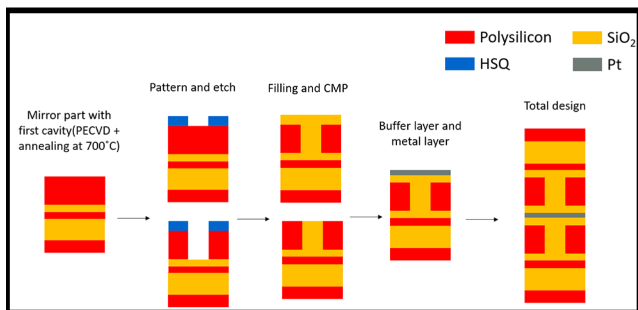

Figure 1: Schematic of the stack structure of the color filter and the main fabrication steps.

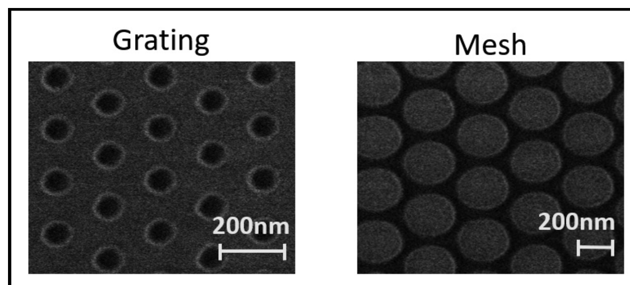

Figure 2: SEM of the mesh and grating structure. The dark part is the HSQ after e-beam lithography and developing. The gray part is polysilicon underneath the HSQ.

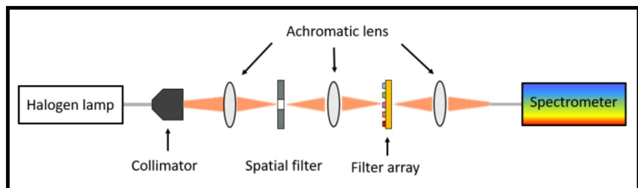

Figure 3: Schematic of the measurement setup.

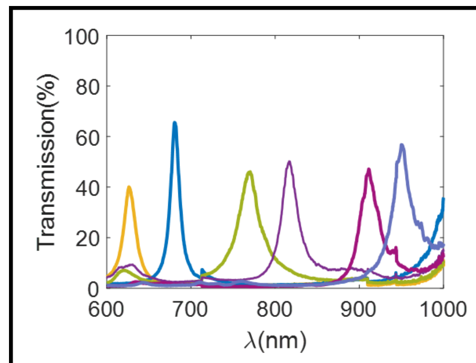

Figure 4: The relative transmission of different color filters based on measurement.

is deposited by plasma-enhanced chemical vapor deposition (PECVD) and anneal it at 700°C for two hours to make it crystalize. We use JEOL 9500 and negative resist hydrogen silsesquioxane (HSQ) to pattern the cavity and use inductively coupled plasma reactive ion etching with HBr to transfer the pattern from HSQ to polysilicon. We fill the gap by atomic layer deposition (ALD) with SiO_2 and polish the surface with chemical mechanical polishing (CMP).

We demonstrate a multispectral color filter array covering from 630 nm to 960 nm with transmissions over 40% and FWHM less than 30 nm. We use a halogen lamp (HL-2000-LL) to generate a broadband light source that covers 400-1700 nm (Figure 3). A collimator and an achromatic lens are used to focus the light on the filter which is 50 µm × 50 µm. We deposit 100 nm Pt above the sample and open a 40 µm × 40 µm aperture on the filter. A blank fused silica wafer with the same apertures is used as the reference. The transmitted light is collected and focused on the spectrometer (Ocean Insight FLAME-S-VIS-NIR-ES). The relative transmission is acquired by comparing the transmission of filters with the reference wafer. From the measurement (Figure 4), the filter array can cover the spectrum from 630 nm to 960 nm with transmission above 40%. The FWHM of all measured transmission peaks is smaller than 30 nm. The transmission and FWHM can be improved by refining the fabrication process to decrease the asymmetry between the two cavities.

Conclusions and Future Steps:

We show that using the sub-wavelength grating, broadband and narrow linewidth color filter array with the same layer structure can be created, which enables monolithic integration of filter banks with imaging sensors. This design can be transferred to visible or infrared wavelength by changing the high index material and optimizing the thickness and lattice structure. This has the promise of a monolithic broadband multispectral color filter array and paves the way for one-shot multi-spectral imaging.

References:

[1] Lapray, P.-J., Wang, X., Thomas, J.-B., and Gouton, P. Multispectral Filter Arrays: Recent Advances and Practical Implementation. Sensors 14, 21626-21659 (2014).

[2] McClung, A., Samudrala, S., Torfeh, M., Mansouree, M., and Arbabi, A. Snapshot spectral imaging with parallel metasystems. Sci. Adv. 6, eabc7646 (2020).

[3] Horie, Y., Arbabi, A., Arbabi, E., Kamali, S. M., and Faraon, A. Wide bandwidth and high resolution planar filter array based on DBR-metasurface-DBR structures. Opt. Express 24, 11677 (2016).

[4] Lee, K.-T., Han, S. Y., Li, Z., Baac, H. W., and Park, H. J. Flexible High-Color-Purity Structural Color Filters Based on a Higher-Order Optical Resonance Suppression. Sci Rep 9, 14917 (2019).

Engineered Second-Order Nonlinearity in Silicon Nitride

CNF Project Number: 2524-17

Principal Investigator(s): Jaime Cardenas

User(s): Yi Zhang

Affiliation(s): The Institute of Optics, University of Rochester

Primary Source(s) of Research Funding: National Science Foundation

Contact: jaime.cardenas@rochester.edu, yzh239@ur.rochester.edu

Website: https://www.hajim.rochester.edu/optics/cardenas/

Primary CNF Tools Used: JEOL 9500, ASML PAS 5500/300C DUV Stepper, Oxford PECVD, AJA Sputter Deposition, LPCVD Furnace, Oxford 100 Etcher, Unaxis 770 Deep Silicon Etcher, Xactix Xenon Difluoride Etcher

Abstract:

We induce a permanent second order nonlinearity of 0.24 pm/V in silicon nitride via electrical poling at a high temperature. We demonstrate electro-optic response usable for modulation in the engineered silicon nitride device up to 15 GHz.

Summary of Research:

Silicon nitride (Si_3N_4) is as a high-performance platform for versatile on-chip photonic devices [1,2] because of its low propagation loss, broad transparency window (400-6700 nm [3]) and good compatibility with complementary metal-oxide semiconductor (CMOS) processing. However, Si_3N_4 lacks an intrinsic second-order nonlinearity ($\chi^{(2)}$) due to its centrosymmetric structure [4]. Building an intrinsic $\chi^{(2)}$ that allows high-speed (gigahertz level) EO response in Si_3N_4 will create a new photonic platform with great potential in integrated photonics.

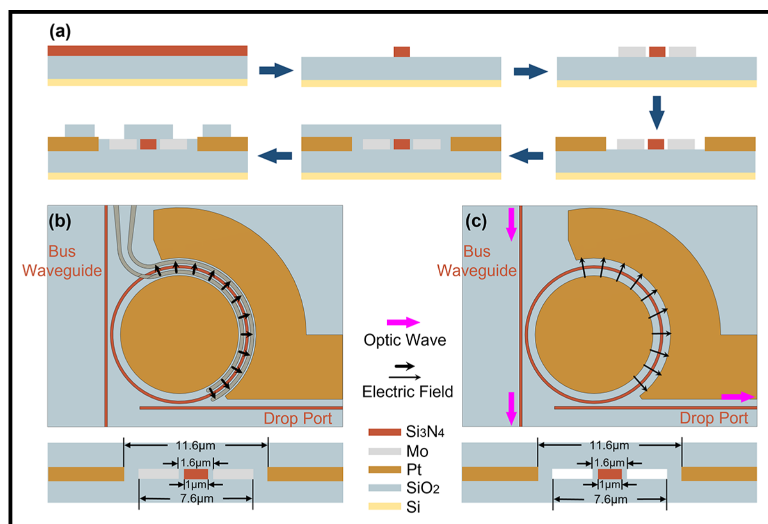

Figure 1: (a) Fabrication procedures of our device. (b) Ring resonator under poling. (c) Ring resonator under high-speed test (Mo removed).

We demonstrate induction of a second-order nonlinearity in Si_3N_4 by electrically poling the film and aligning the Si-N bonds. Khurgin, et al. [5] hypothesized that the Si-N bonds in Si_3N_4 possess a second-order hyperpolarizability comparable to Ga-As bonds in GaAs, whose $\chi^{(2)}$ is as large as 300 pm/V. The centrosymmetric orientation of the Si-N bonds causes their contribution to cancel each other and leads to a bulk $\chi^{(2)}$ of zero. However, by aligning these bonds and breaking the symmetry, even slightly, a non-trivial intrinsic $\chi^{(2)}$ will naturally emerge and thus induce a high-speed EO response in Si_3N_4.

We use an Si_3N_4 ring resonator (1μm*300nm) with electrodes to study the EO response in poled and non-poled Si_3N_4. Fabrication procedures are shown in Figure 1(a). We deposit 300 nm LPCVD nitride over 4 μm thermally-grown oxide on a silicon wafer. The waveguide is patterned using e-beam lithography and etched using reactive-ion etching (RIE). We then pattern a pair of Mo electrodes using DUV lithography and deposit the metal through sputter-liftoff process. This pair of electrodes is placed 300 nm away from the waveguide (edge to edge) to generate a strong electric field to pole the Si_3N_4 ring (Figure 1(b)).

We choose Mo as the material since it can be removed using XeF_2 after poling to eliminate the huge loss it introduces to the ring, which we need for characterization of the EO response, which has a high selectivity to all the other materials used in the device.

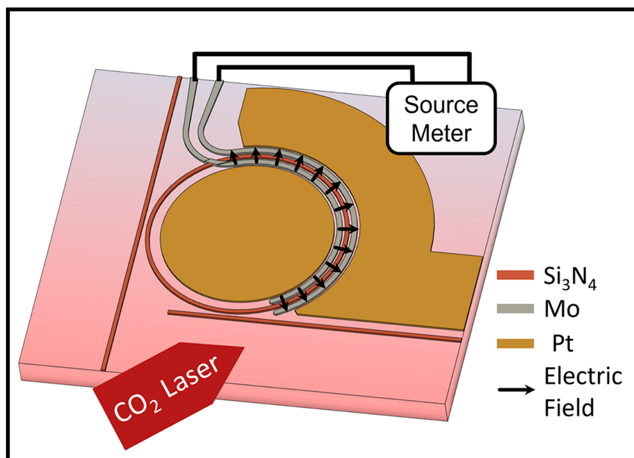

Figure 2: Poling of Si_3N_4 ring resonator heated by CO_2 laser beam.

Another pair of platinum (Pt) electrodes is then patterned and deposited in the same way outside the Mo ones for EO modulation after the removal of Mo (Figure 1(c)). Afterwards, we clad the waveguide and electrodes with 2 µm PECVD oxide and open vias for probe contact and XeF_2 etching.

We heat up the device to facilitate the poling process [6] by focusing a 10W CO_2 laser beam beside the ring (Figure 2). We limit the heating to 700°C as we observe rapid dropping of the arcing threshold between the electrodes, which limits the field strength we can apply, when going to higher temperature. After reaching this desired temperature, we apply a high voltage to the Mo electrodes for poling. The maximum voltage we manage to apply without arcing is 160V and it corresponds to a horizontal poling field of 0.68 MV/cm in Si_3N_4 according to simulation. The device sinks in the high temperature poling for five minutes before we disable the heating laser. The poling field is maintained until the device cools down to room temperature (in a few seconds). Such rapid cooling helps to freeze the aligned bonds in their new positions and prevent them from rolling back (as the poling field still remains).

We quantitively characterize the r_{33} and r_{31} EO coefficients of the Si_3N_4 resonator (Figure 3(a)). The measured values at different working frequencies for the poled device (red lines, various time after poling) and non-poled reference (green line) are shown in Figure 3 (b-c). We observe that the poled device demonstrates an enhancement of the r_{33} component to 30 fm/V (effective $\chi^{(2)}$ 240 fm/V [4]). After the poling the speed of the measured EO response increases. The reference device shows a 3dB cutoff frequency of 3 GHz (data points at high frequencies have their lower error bar set to zero since they are hardly distinguishable from the background noise), while this number improves to at least 15 GHz for the poled device, for both r_{33} and r_{31} component. The *slow response* measured in the non-poled device is a result of carrier-related effects in Si_3N_4 as previously reported [7], which has a speed limit of approximately 1 GHz [8]. The *fast response* of the poled device, on the other hand, confirms our induction of a second-order nonlinearity in the poled Si_3N_4 as no other mechanism can enable EO response of such high speed. We track the EO response in the poled device for one week and observe no significant decay, suggesting our induction is long-lasting and permanent.

Conclusions and Future Steps:

In conclusion, we demonstrate a permanent second-order nonlinearity of 0.24 pm/V and corresponding electro-optic response as fast as 15 GHz built in silicon nitride through electrical poling. This work paves the way to enabling high-speed active functions on the Si_3N_4 platform, substantially expanding its potential applications.

References:

[1] D. J. Blumenthal, R. Heideman, D. Geuzebroek, A. Leinse, and C. Roeloffzen, Proceedings of the IEEE 106, 2209-2231 (2018).

[2] P. Muñoz, et al. Sensors 17, 2088 (2017).

[3] R. Soref, Nature Photon 4, 495-497 (2010).

[4] R. W. Boyd, Nonlinear Optics (Academic Press, 2020).

[5] J. B. Khurgin, T. H. Stievater, M. W. Pruessner, and W. S. Rabinovich, J. Opt. Soc. Am. B 32, 2494 (2015).

[6] R. A. Myers, N. Mukherjee, and S. R. J. Brueck, Opt. Lett. 16, 1732 (1991).

[7] S. Sharif Azadeh, F. Merget, M. P. Nezhad, and J. Witzens, Opt. Lett. 40, 1877 (2015).

[8] M. Borghi, et al. Opt. Lett. 40, 5287 (2015).

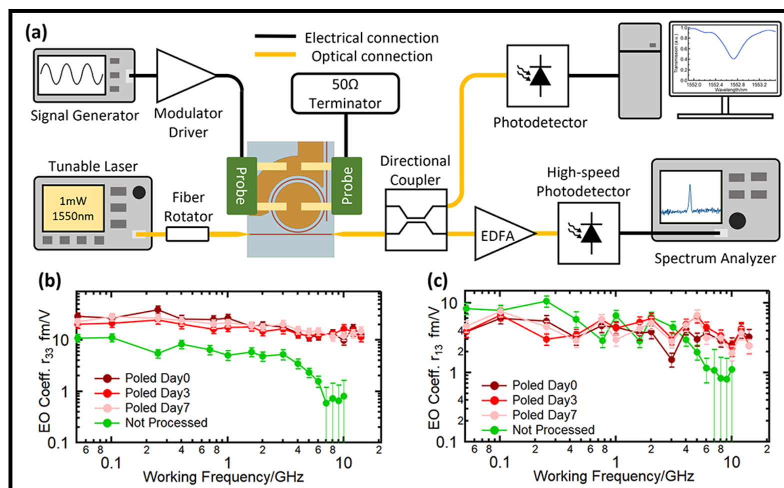

Figure 3: (a) Schematic of apparatus of EO response characterization. (b-c) Measured EO coefficient r_{33}(b) and r_{13}(b) at various frequencies of both poled and non-poled device.

A Low SWaP, Robust, High Performance Hyperspectral Sensor for Land and Atmospheric Remote Sensing

CNF Project Number: 2661-18

Principal Investigator & User: Lori Lepak

Affiliation(s): Phoebus Optoelectronics LLC

Primary Source(s) of Research Funding: National Aeronautics and Space Administration (NASA)

Contact: llepak@phoebusopto.com

Website: www.phoebusopto.com

Primary CNF Tools Used: ASML DUV Stepper, Oxford 81 Etcher, Logitech CMP, Supra SEM

Abstract:

Since 2003, Phoebus Optoelectronics LLC has enabled custom R&D solutions in the fields of Plasmonics, Metamaterials, Antennas, and Sensors. We work closely with our customers throughout device development, from simulation and design, to prototype realization, testing, and small volume manufacturing. Our R&D portfolio spans the spectral ranges of visible light, infrared, terahertz, and microwave radiation, for applications in high resolution imaging systems, wavelength and polarization filtering, tunable optical components, beam forming and steering, solar cells, renewable energy devices, and chemical and biological toxin sensors. We routinely partner with large, industry-leading businesses to develop products in all of these areas, jointly performing advanced testing and working together to scale up to medium- and large-volume manufacturing.

Our agile team makes extensive use of the resources at the CNF for our nano/micro fabrication and testing, to provide cost efficiency and rapid turnaround.

In the present report, we discuss the ongoing development of a metamaterial-based hyperspectral imaging filter.

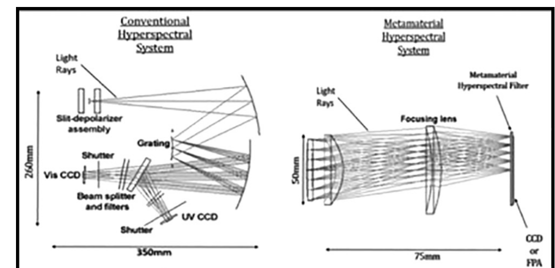

Figure 1: Phoebus's Metamaterial Spectrometer (MS) technology (right) eliminates much of the size and weight of conventional hyperspectral spectrometer technologies (left). Note the significant difference in scale of the two images.

Summary of Research:

Phoebus Optoelectronics uses the resources of the CNF to fabricate plasmonic chips patterned with a metamaterial surface to enable Extraordinary Optical Transmission (EOT), a phenomenon unique to metastructures in which light is transmitted through apertures much smaller than the incident wavelength, at anomalously large intensities relative to the predictions of conventional aperture theory. EOT was first observed by T.W. Ebbesen in 1998 [1]. Since its founding in 2003, Phoebus has successfully harnessed EOT by incorporating metasurfaces into devices used to perform light filtering [2,3], photon sorting [4,5], polarimetric detection [6], high speed optical detection [7], and SPR plasmonic sensor chips [8].

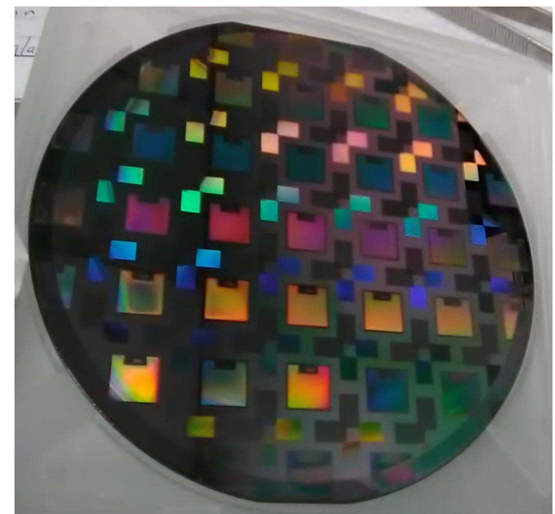

Figure 2: Wafer lithographically patterned with optical metastructures, using the ASML DUV stepper.

In our current project, we are developing a hyperspectral imaging system, shown schematically in Figure 1. Our technology (Figure 1b) uses a metasurface to precisely target very narrow spectral bands of interest, enabling a significant reduction in the size and number of optical components relative to current state-of-the-art imaging systems (Figure 1a), which in turn will enable the integration of our high-performance sensor onto weight-sensitive platforms (i.e., satellites) far more readily than existing systems. Our initial goal is to detect and image trace gases in the Earth's atmosphere in the midwave infrared (MWIR), defined as 3-5 µm

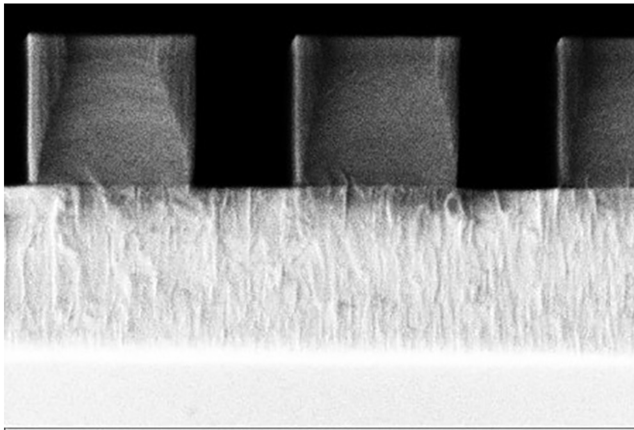

Figure 3: SEM image (cross section) of etched pillars with near-vertical sidewalls. Imaged at ~ 90 kX in the Supra SEM, the grain structure of the etch stop layer is clearly visible.

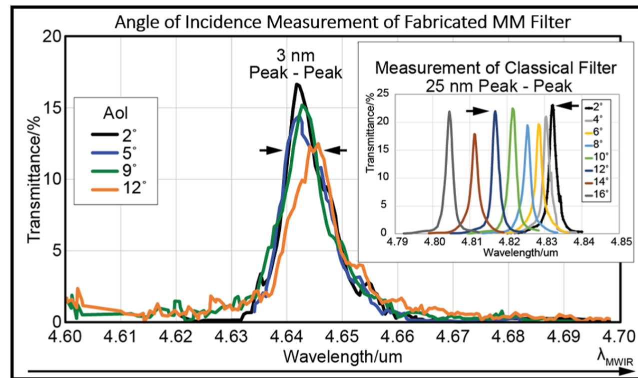

Figure 4: Measured optical performance of fabricated metamaterial filter showing the angle of incidence independence up to a cone of 12° (f/2.4). (Inset) Same measurement performed on a classical Fabry-Pérot filter. Reproduced from reference 9.

wavelength, while minimizing dependence on the Angle of Incidence (AoI) of light upon the sensor, up to an angle of 12° off-normal.

Using the ASML DUV stepper, entire wafers can rapidly be lithographically patterned with highly uniform, large-area arrays of metastructures, as shown in Figure 2. In general, the optimal feature size and period of these metastructures depends primarily upon the desired wavelength of operation and the refractive indices of the constituent materials. In the MWIR, typical feature sizes are on the order of ~ 1 µm. Equally critical for minimizing optical losses in photonics applications, the relatively narrow spaces between features can be etched to form high-aspect-ratio structures with nearly vertical sidewalls, as shown in Figure 3.

Conclusions and Future Steps:

With strong, ongoing support from the National Aeronautics and Space Administration (NASA), we have successfully tested our second generation MWIR devices. As shown in Figure 4, they demonstrated the desired AoI insensitivity up to 12°. Having identified a few key areas for process improvements, we are currently fabricating a third generation, to fully optimize and pixelate our MWIR device. In addition, we are adapting our metasurface technology to other spectral ranges, from the visible to the microwave, by substituting appropriate materials, and scaling feature sizes as appropriate to the imaging wavelength.

In particular, we developing a second generation of a visible/NIR-wavelength counterpart of the current technology. The NIR/vis devices are fabricated using all of the same tools as the MWIR project, plus the Oxford PECVD and AJA sputter tool to deposit thin films. Thus, the extensive resources of the CNF are enabling us to rapidly develop our Metamaterial Spectrometer technology for a broad range of imaging and sensing applications.

References:

[1] Ebbesen, T.W., et al., "Extraordinary optical transmission through sub-wavelength hole arrays." Nature, (1998). 391(6668): p. 667-669.

[2] Crouse, D. "Numerical modeling and electromagnetic resonant modes in complex grating structures and optoelectronic device applications." Electron Devices, IEEE Transactions on 52.11 (2005): 2365-2373.

[3] Crouse, D., and Keshavareddy, P. "Polarization independent enhanced optical transmission in one-dimensional gratings and device applications." Optics Express 15.4 (2007): 1415-1427.

[4] Lansey, E., Crouse, D., et al. "Light localization, photon sorting, and enhanced absorption in subwavelength cavity arrays." Optics Express 20.22 (2012): 24226-24236.

[5] Jung, Y.U; Bendoym, I.; Golovin, A.B.; and Crouse, D.T. "Dual-band photon sorting plasmonic MIM metamaterial sensor." Proc. SPIE 9070, Infrared Technology and Applications XL, 90702X (June 24, 2014); doi:10.1117/12.2050620.

[6] Crouse, D., and Keshavareddy, P. "A method for designing electromagnetic resonance enhanced silicon-on-insulator metal–semiconductor–metal photodetectors." Journal of Optics A: Pure and Applied Optics 8.2 (2006): 175.

[7] Mandel, I.; Gollub, J.; Bendoym, I; Crouse, D. Theory and Design of A Novel Integrated Polarimetric Sensor Utilizing a Light Sorting Metamaterial Grating. Sensors Journal, IEEE, (2012): Vol. PP, 99.

[8] Lepak, L., et al. "Handheld chem/biosensor using extreme conformational changes in designed binding proteins to enhance surface plasmon resonance (SPR)" Proc. SPIE 9862, Advanced Environmental, Chemical, and Biological Sensing Technologies XIII, 9862-7 (April 17, 2016); doi:10.1117/12.2222305.

[9] Bendoym, I., Lepak, L., Leitch, J., Applegate, J., Crouse, D. "Low SWaP-C hyperspectral metamaterial spectrometer (MMS) for narrow-band, wide angle-of-incidence MWIR atmospheric sensing," Proc. SPIE 12091, Image Sensing Technologies: Materials, Devices, Systems, and Applications IX, 120910J (30 May 2022); https://doi.org/10.1117/12.2632794.

OWiC microLINKs: Microscopic Optical Smart Tags for Connecting Digital Content to the Physical World

CNF Project Number: 2909-20

Principal Investigator(s): Alejandro Cortese[1], Paul L. McEuen[1], Alyosha Molnar[1], Robert Scharf[2]

User(s): Alejandro Cortese

Affiliation(s): 1. OWiC Technologies, Inc.; 2. Praxis Center for Venture Development

Primary Source(s) of Research Funding: NSF SBIR Phase I Award Number 2014984

Contact: alejandro@owictech.com, pmceuen@gmail.com, amolnar@owictech.com, rms248@cornell.edu

Primary CNF Tools Used: Heidelberg Mask Writer - DWL2000, ABM Contact Aligner, Zeiss SEMs, Oxford 100 ICP Etcher, Oxford 81 Etcher, Oxford Cobra Etcher, PT770 Etcher, AJA Sputter Deposition, Oxford PECVD, SC4500 Evaporator, Oxford ALD

Abstract:

OWiC Technologies is a Cornell spinout startup commercializing a new class of unique ID tags called microLINKs to securely, intelligently, and wirelessly connect the physical and digital worlds. The microLINKs tags are based on the core technology of Optical Wireless Integrated Circuits (OWiCs), that are effectively in-visible, intelligent, and integrated with a built-in optical power and communication system made of photovoltaics/microLED. A microLINK tag functions in a way analogous to an RFID tag but uses light for power and communication instead of RF. When light is directed toward a microLINK, it will blink out a unique 64-bit ID that can be read out with a handheld reader. The code, in conjunction with a cloud database of tags and links, connects to digital content on a smartphone, tablet, or, in the future, smart glasses. We use a wide range of tools in the Cornell NanoScale Facility (CNF) to produce these microLINK tags.

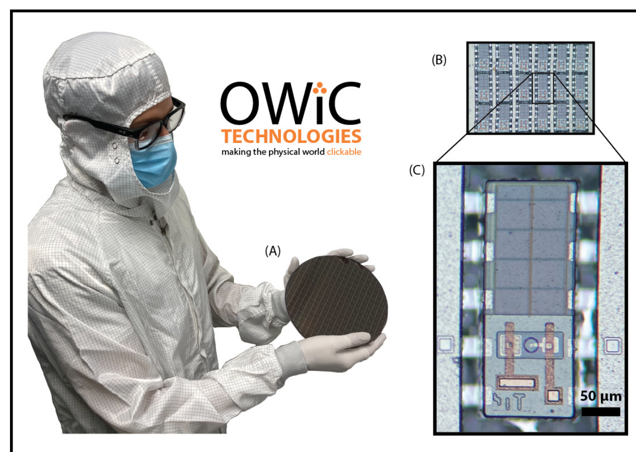

Figure 1: (A) An 8-inch wafer of microLINK integrated circuits from a commercial foundry. (B) An array of integrated microLINK tags. (C) An integrated microLINK tag prior to removal from the substrate. This microLINK tag design is approximately 100 × 300 microns.

Summary of Research:

The entire microLINK device is approximately 100 × 300 microns in size and is composed of photovoltaics, a circuit for on board digital logic, and a microLED. The photovoltaics and integrated circuit are designed in a 180 nm silicon-on-insulator (SOI) complementary metal-oxide-semiconductor (CMOS) process available from a commercial foundry. The circuit creates a series of electrical pulses that encode a unique identification code that are used to drive the microLED, producing the output light. These circuits are received from the commercial foundry as a wafer shown in Figure 1(A). Separately, we produce light emitting elements in the CNF primarily out of gallium arsenide heterostructures. These two components — the CMOS components and microLED — are then integrated using heterogenous integration methods. Methods for producing these devices are detailed in references below [1-4].

Figure 1 A shows an array of integrated microLINK devices before being removed from the substrate is shown in Figure 1 (B) as well as a zoomed in image of a single device, Figure 1 (C).

References:

[1] A. C. Molnar, S. Lee, A. Cortese, P. McEuen, S. Sadeghi, S. Ghajari, in 2021 IEEE Custom Integrated Circuits Conference (CICC) (2021), pp. 1-6.

[2] S. Lee, A. J. Cortese, A. P. Gandhi, E. R. Agger, P. L. McEuen, A. C. Molnar, A 250 µm × 57 µm Microscale Opto-electronically Transduced Electrodes (MOTEs) for Neural Recording. IEEE Trans. Biomed. Circuits Syst. 12, 1256-1266 (2018).

[3] S. Lee, A. J. Cortese, A. Mok, C. Wu, T. Wang, J. U. Park, C. Smart, S. Ghajari, D. Khilwani, S. Sadeghi, Y. Ji, J. H. Goldberg, C. Xu, P. L. McEuen, A. C. Molnar, Fabrication of Injectable Micro-Scale Opto-Electronically Transduced Electrodes (MOTEs) for Physiological Monitoring. J. Microelectromechanical Syst. 29, 720-726 (2020).

[4] A. J. Cortese, C. L. Smart, T. Wang, M. F. Reynolds, S. L. Norris, Y. Ji, S. Lee, A. Mok, C. Wu, F. Xia, N. I. Ellis, A. C. Molnar, C. Xu, P. L. McEuen, Microscopic sensors using optical wireless integrated circuits. Proc. Natl. Acad. Sci. 117, 9173-9179 (2020).

Electrical and Optical Characterization of Thin Film Silicon-Rich Nitride

CNF Project Number: 2971-21

Principal Investigator(s): Peter McMahon[1,2]

User(s): Tatsuhiro Onodera[1,3], Martin Stein[1,3]

Affiliation(s): 1. School of Applied and Engineering Physics, Cornell University, Ithaca, NY 14853, USA; 2. Kavli Institute at Cornell for Nanoscale Science, Cornell University, Ithaca, NY; 3. NTT Physics and Informatics Laboratories, NTT Research, Inc., Sunnyvale, CA, USA

Primary Source(s) of Research Funding: National Science Foundation (award CCF-1918549), David and Lucile Packard Foundation Fellowship, NTT Research

Contact: pmcmahon@cornell.edu, to232@cornell.edu, ms3452@cornell.edu

Primary CNF Tools Used: Oxford 100 PECVD, E-Beam Evaporator, Woollam RC2 Spectroscopic Ellipsometer, Metricon 2010/M Prism Coupler

Abstract:

Silicon-rich silicon nitride (SRN) has recently attracted attention for its promise to enable high-power nonlinear optical information processing. The same qualities that make SRN promising for this application—a large optical nonlinearity and high dielectric strength—also make SRN a promising material for programmable integrated photonics. To demonstrate this potential, we fabricated low loss SRN films with a large electro-optic effect and show that the material's electrical properties are extremely versatile and can be optically controlled.

Summary of Research:

We characterized electrical and optical properties of thin silicon-rich silicon nitride (SRN) PECVD films with different silicon and nitrogen contents. SRN is a class of materials with a bandgap ranging between that of stoichiometric silicon nitride (SiN) and amorphous silicon. This makes SRN generally more electrically insulating than silicon but more conductive than SiN. Its optical properties similarly range between those of silicon and SiN, with a refractive index from about 2 to 3.5 at 1550 nm, increasing with higher silicon content, and a large Kerr nonlinearity.

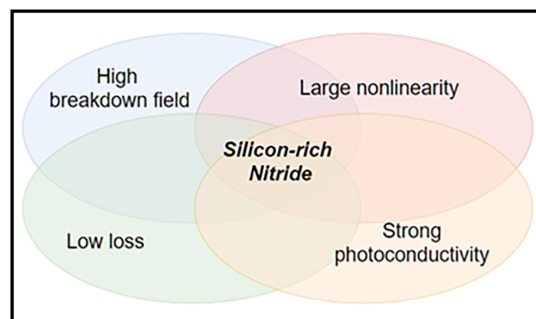

Figure 1: Silicon-rich nitride combines several desirable material properties for programmable photonic circuits. The combination of a high breakdown field [2] and large nonlinear coefficients allows large refractive index modulations [1,3]. A strong photoconductivity allows modulating the electro-optic effect with visible light while low losses [4] are a prerequisite for deep photonic circuitry.

We measured the electrical conductivity of different SRN films by measuring the I-V characteristics under different conditions and we measured the propagation loss of light at 1550 nm in SRN slab waveguides using prism coupling, as well as the electro-optic effect at 1550 nm.

Electrical Conductivity. To measure the electrical conductivity, we deposited around 500 nm thick SRN layers of different silicon content using PECVD on strongly p-type Si wafers. The gas flow ratios for the different materials were varied from 40 sccm SiH_4, 10 sccm NH_3 and 1425 sccm N_2 for the material closest to SiN (lowest refractive index and lowest conductivity) to 25 sccm SiH_4 and no NH_3 or N_2 for the material closest too amorphous silicon (highest index and most conductive). We then deposited 15 nm titanium and 15 nm gold electrodes on top of the SRN layer. We inferred the conductivity from the current flowing when applying a negative bias to the gold electrode and keeping the substrate at ground. We repeated the measured while illuminating the chips with approximately 100 mW/cm^2 at 530 nm.

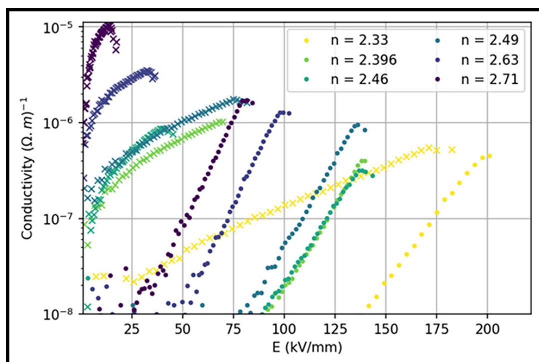

Figure 2: Conductivity of different silicon-rich nitrides as a function of electric field and illumination. Different colors correspond to different gas flow rates of SiH_4 and NH_3, ranging from 4:1 (n=2.33) to >10:1 (n=2.71). Different markers correspond to different illuminations: Dots mark the conductivity in the dark state, "x"s mark the conductivity in the bright state under approximately 100 mW/cm² of 530 nm light. The saturation at the top of each conductivity curve is an artifact from the compliance current of our high voltage amplifier.

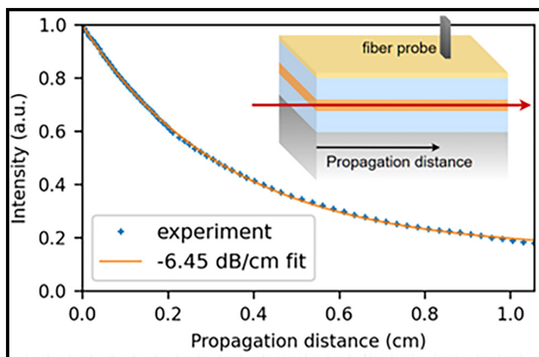

Figure 3: Measurement of optical propagation loss in SRN slab waveguide. The waveguide consists of a 500 nm thick SRN core with refractive index of 2.45 at 1550 nm (SiH_4:NH_3 gas ratio of 6) and 700 nm thick SiO_2 claddings on each side. The loss is estimated by measuring scattered light on top of the waveguide as a function of propagation distance using the Metricon 2010/M prism coupler. An exponential fit yields a loss of 6.45 dB/cm.

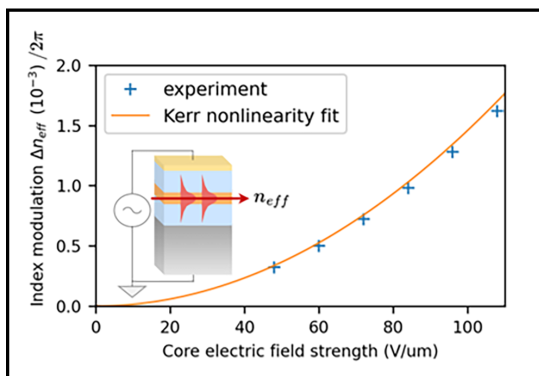

Figure 4: Measurement of the electro-optic response of the SRN waveguide from Figure 3 at 1550 nm. We applied a 10 Hz AC voltage across the waveguide stack. The electric field strength in the core was estimated using the conductivity measurements from Figure 2. The refractive index modulations were measured using an interferometer. A part of the 1550 nm beam was splitted off before entering the waveguide, routed around the waveguide and then recombined with the beam going through the waveguide. We established the refractive index modulations of the waveguide from the resulting interference fringes. The measured index modulations are consistent with a Kerr nonlinearity.

The results are shown in Figure 2. SRN is generally very resistive with conductivities ranging from 10.8 to 10.5Ω cm, but the conductivity is very sensitive to the silicon content (as evident from the refractive index), applied voltage, and can change more than three orders of magnitude from bright to dark state.

Optical Properties. We measured the refractive index of SRNs with different silicon content. Representatively shown in Figure 3 is a measurement of the optical propagation loss of a 1550 nm beam in a 500 nm thick slab of SRN with 700 nm SiO_2 claddings. The loss was much higher than expected from ellipsometer measurements of the extinction coefficient, so we believe the loss is largely due to surface roughness. We also observed a photo-induced loss of yet unknown origin when illuminating the waveguide with visible light. This loss is about 3 dB/cm and might be due to the photoconductivity shown in Figure 2.

We measured the electro-optic modulation by measuring the change in effective refractive index when applying an electric field across the waveguide. As seen in Figure 4, the relation between refractive index and applied field is quadratic, suggesting a Kerr nonlinearity.

Conclusions and Outlook:

We have characterized silicon-rich silicon nitride films for its applications as a controllable electro-optic material. While lower losses (e.g. [4]) and stronger optical nonlinearities (e.g. [3]) in SRN have been demonstrated before, we also show strong photoconductivity. Although our work is preliminary and should not be treated as definitive, we believe SRN is a promising material for optically programmable photonics.

Acknowledgements:

PLM gratefully acknowledges financial support from a David and Lucile Packard Foundation Fellowship. The authors wish to thank NTT Research for their financial and technical support, and the National Science Foundation (award CCF-1918549). This work was performed in part at the Cornell NanoScale Facility, a member of the National Nanotechnology Coordinated Infrastructure (NNCI), which is supported by the National Science Foundation (Grant NNCI-2025233).

References:

[1] Tan, D. T. H., K. J. A. Ooi, and D. K. T. Ng. "Nonlinear optics on silicon-rich nitride—a high nonlinear figure of merit CMOS platform." Photonics Research 6.5 (2018): B50-B66.

[2] Piccirillo, A., and A. L. Gobbi. "Physical-electrical properties of silicon nitride deposited by PECVD on III–V semiconductors." Journal of The Electrochemical Society 137.12 (1990): 3910.m.

[3] Friedman, Alex, et al. "Demonstration of the DC-Kerr effect in silicon-rich nitride." Optics Letters 46.17 (2021): 4236-4239.

[4] Lacava, Cosimo, et al. "Si-rich silicon nitride for nonlinear signal processing applications." Scientific reports 7.1 (2017): 1-13.

Visible-Light Metasurfaces Based on Silicon-Rich Silicon Nitride

CNF Project Number: 2979-21

Principal Investigator(s): Gennady Shvets

User(s): Melissa Bosch

Affiliation(s): School of Applied and Engineering Physics, Department of Physics; Cornell University

Primary Source(s) of Research Funding: Office of Naval Research (ONR), National Science Foundation (NSF)

Contact: gs656@cornell.edu, mb2583@cornell.edu

Website: http://shvets.aep.cornell.edu

Primary CNF Tools Used: JEOL 9500, Zeiss Ultra SEM, Oxford 100 Etcher, Oxford PECVD, Woollam RC2 Ellipsometer

Abstract:

Optical metasurfaces, consisting of planar arrangements of lithographically-defined subwavelength scatterers, offer a highly compact and scalable alternative to conventional freespace refractive optical elements. We report on the fabrication 500 nm thick silicon-rich silicon nitride (SRN) metasurfaces exhibiting tunable optical resonances, fit for various photonic applications requiring visible light modulation. For example, we integrate SRN-metasurfaces with liquid crystals (LCs) to demonstrate voltage-controlled zoom lenses operating at red/green/blue (RGB) wavelengths. Their scalability, ultrathin-profile, and CMOS-compatibility renders SRN-metalenses uniquely poised to benefit RGB imaging technologies such as augmented reality and depth perception devices.

Summary of Research:

I. Silicon-Rich Silicon Nitride (SRN) Metasurfaces. Metasurfaces have drawn considerable interest over the past decade owing to their widespread potential applications. Semiconductor and dielectric metasurfaces are especially promising platforms for efficient light modulation owing to their low Ohmic losses and support of localized Mie-type resonance modes which are spectrally-sensitive to the permittivity of the media adjacent to the metasurface array [1]. Typically, metasurfaces working at visible wavelengths are composed of GaP or TiO_2, requiring costly and time-consuming deposition processes (i.e., metal-organic chemical vapor deposition and atomic layer deposition) [2,3]. Our project focuses on the PECVD-based fabrication of SiN_x metasurfaces with sub-100 nm feature sizes and moderate (1:4) aspect ratios. Our ellipsometric characterization of PECVD-deposited SiN_x thin films shows flexible control over the films' refractive index and extinction coefficient through variations in the SiH_4:NH_3 gas ratio (Figure 1). Several gas ratios yield SRN films exhibiting low extinction coefficients and acceptable refractive indices at RGB wavelengths: fit for use as the constituent material of visible-light metasurfaces. A scanning electron microscope (SEM) image of a representative SRN metasurface is shown in Figure 2, consisting of an array of rectangular SRN resonators on a silica substrate, where the spacing between neighboring resonators governs the bandwidth of the optical resonance. The SRN devices are fabricated using plasma-enhanced chemical vapor deposition (Oxford PECVD) of SRN onto a fused silica substrate; HSQ 6% spin-coat, baking, and e-beam exposure at 7.5 mC/cm^2 (JEOL 9500FS); development in TMAH/NaCl (0.25/0.7N) salty solution; and pattern transfer to the SRN layer through reactive ion etching (Oxford 100). The fabricated samples were characterized with a scanning electron microscope (Zeiss Ultra), showing good accuracy of geometric dimensions.

II. Tunable-Focus Lens Using a Liquid-Crystal-Embedded SRN-Metasurface. In one application, we utilize PECVD SRN films to create a SRN-metalens behaving as a visible-light lens with voltage-actuated zoom. Metalenses with tunable focal lengths offer many advantages to contemporary vision and imaging systems; however, most metalenses have static focal lengths after fabrication. Our previous work used amorphous silicon metasurfaces infiltrated with liquid crystals (LCs) to demonstrate a varifocal metalens with voltage-actuated focal length in the infrared [2].

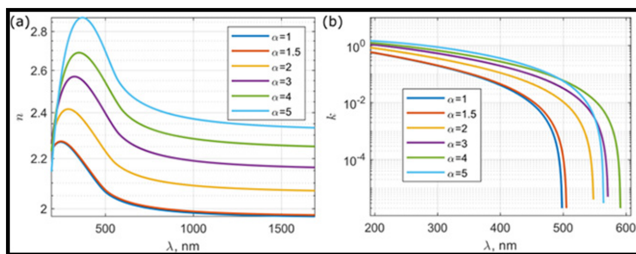

Figure 1: (a) Refractive index n and (b) extinction coefficient k of PECVD-deposited SRN films as a function of the SiH_4:NH_3 gas ratio α and wavelength λ.

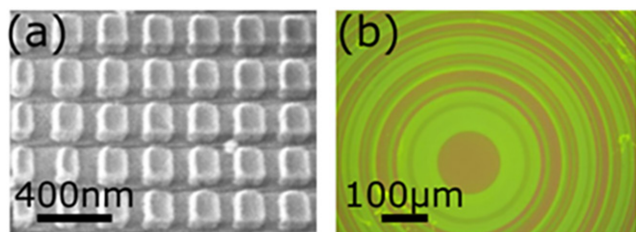

Figure 2: (a) A scanning electron microscopy (SEM) image of a representative SRN-metasurface, consisting of a periodic array of rectangular SRN pillars on a silica substrate. (b) Optical microscope image of the fabricated 1.5-mm-diameter spherical SRN-metalens. The different colors of the concentric rings of the metalens correspond to unique metasurface pillar geometries.

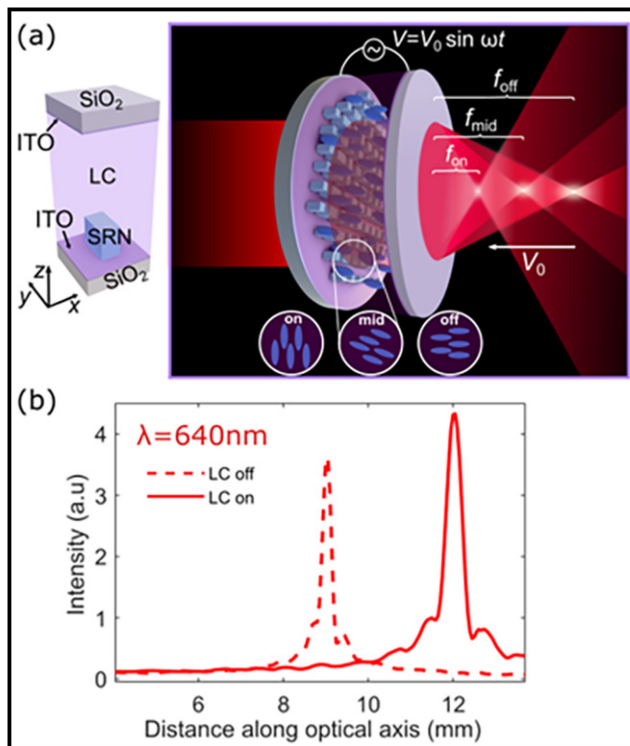

Figure 3: Left: The metasurface unit cell, consisting of a rectangular SRN meta-atom embedded in a LC and sandwiched between two transparent conducting indium-tin-oxide (ITO)-coated silica plates. Right: An AC voltage applied across electrodes modulates the LC molecule orientation and resulting focal length of the metalens. (b) Simulated intensity of transmitted light along the optical axis of the SRN-metalens for λ = 640 nm. The lens acts as a converging lens with a 9 mm focal length in the absence of an external electric field (dashed red line) and a 11 mm focal length in the presence of an external electric field (solid red line).

We merge this design strategy with SRN thin film engineering to design and fabricate SRN-based resonant LC-metalenses (Figure 2b) that enables switchable-focus at visible wavelengths. The metasurface unit cell is a rectangular SRN pillar embedded in a nematic LC and sandwiched between two conductive plates, as shown in Figure 3a. The local phase response of the SRN meta-atoms are modulated by means of the field-dependent LC, resulting in continuous and reversible modulations of the metalens focal length. In one design for red light meta-atom geometries are optimized to impart phase shifts that approximate the ideal focusing phase profile for a converging lens with focal distance $f = f_{off}$ in the LC "off" state, while simultaneously engineered to impart the phase profile of a converging lens with $f = f_{on}$ in the LC "on" state. To validate the approach, we fabricated a 1.5-mm-diameter spherical metalens that facilitates voltage-actuated switching between two distinct focal distances of f_{off} = 9 mm and f_{on} = 11 mm at a wavelength of 640 nm. Our simulations at predict high-contrast switching between focal spots in response to the "off"-to-"on" permittivity modulation of the LC, as shown in Figure 3b.

References:

[1] Genevet, Patrice, et al. "Recent advances in planar optics: from plasmonic to dielectric metasurfaces." Optica 4.1 (2017): 139-152.

[2] Devlin, Robert C., et al. "Broadband high-efficiency dielectric metasurfaces for the visible spectrum." Proceedings of the National Academy of Sciences 113.38 (2016): 10473-10478.

[3] Grinblat, Gustavo, et al. "Efficient ultrafast all-optical modulation in a nonlinear crystalline gallium phosphide nanodisk at the anapole excitation." Science advances 6.34 (2020).

[4] Bosch, Melissa, et al. "Electrically actuated varifocal lens based on liquid-crystal-embedded dielectric metasurfaces." Nano Letters 21.9 (2021): 3849-3856.

Development of Visible Light/IR Diffractive Optical Elements for Beam Shaping Using Nanoimprint Lithography

CNF Project Number: 3024-22
Principal Investigator(s): Keiko Munechika
User(s): Kaito Yamada

Affiliation(s): HighRI Optics, Inc., Oakland, California, USA

Primary Source(s) of Research Funding: HighRI Optics, Inc.

Contact: km@highrioptics.com, kaitoy@highrioptics.com
Website: https://highrioptics.com

Primary CNF Tools Used: Nanonex NX-2500

Abstract:

The development process in nanoimprint lithography is a key piece of technology for optical device fabrications, such as Diffractive Optical Elements. Our developed UV curable resins with refractive indices of 1.8-2.0 have now been successfully imprinted without any defects. This technology will not only improve the device performance, but also expand the applications of nanoimprint lithography for use with an array of optical devices.

Summary of Research:

Many fields have begun looking to the development of nanofabrication technologies to achieve better resolution, improved variation of critical dimensions, and improved placement accuracy in their technology. Nanoimprint lithography has shown to be a promising avenue from which to accomplish these goals at a low cost, for a wide variety of consumer applications [1]. However, the development process can be quite challenging since the optimized conditions vary depending on the mold design and chosen materials.

Applications for Diffractive Optical Elements (DOEs) have attracted a lot of attention, as they can implement versatile functionalities such as beam shaping and phase encoding [2]. For such applications, high refractive index materials are highly sought after to improve the performance of these devices. HighRI Optics is developing a series of high refractive index nanoimprint resins with the refractive index n ~ 1.8-2.0, representing one of the highest commercially available RI values [3]. Here we report on the successful fabrication of DOEs using our developed materials with a refractive index of up to 2.0.

Silicon or fused silica wafers were spin-coated with the high refractive index materials, and nanoimprint lithography was performed using Nanonex NX-2500 as shown in Figure 1. Following UV exposure, the master mold was demolded from the UV resin layer to achieve the desired replicated patterns. Figure 2 shows an image

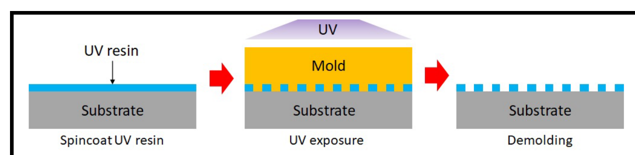

Figure 1: A schematic of nanoimprint lithography.

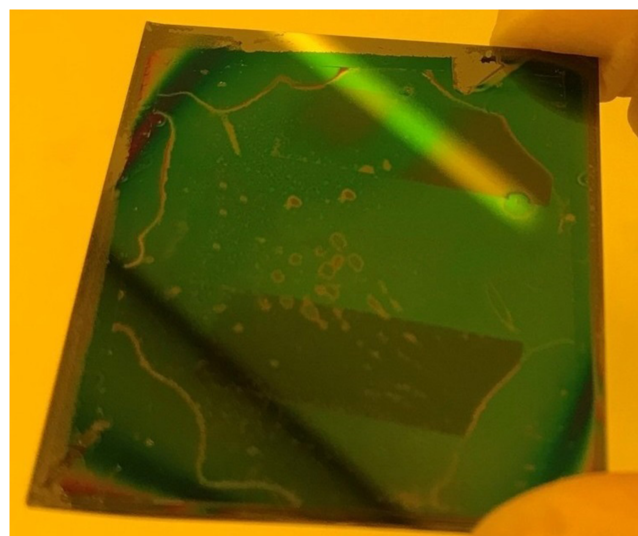

Figure 2: Imprinted patterns in the high refractive index polymer with many defects.

OPTICS & OPTO-ELECTRONICS

of the imprinted patterns fabricated in our facility, and Figure 3 displays an image of the same patterns fabricated at CNF. The results clearly show an increase in the quality of the imprinted patterns, and no defects were observed on the device.

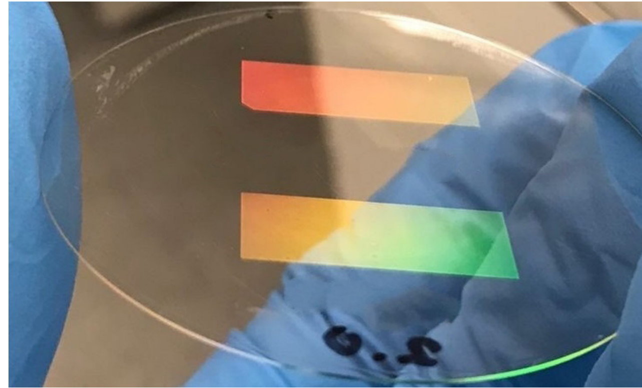

Figure 3: Imprinted patterns in the high refractive index polymer with no defects.

Conclusions and Future Steps:

By optimizing the imprint conditions, our developed materials with high refractive index have been successfully imprinted with the necessary patterns for DOE applications. This technology is expected to greatly improve the performance of DOEs for versatile applications such as augmented reality and virtual reality devices. Our next steps are to continue optimizing the fabrication process to suit more complex designs, as well as to further increase the refractive index of the materials.

References:

[1] S. Chou, P. R. Krauss, and P. J. Renstrom, Science, 272, 5258, 85 (1996).

[2] A. Siemion, Sensors, 21, 100 (2021).

[3] C. Pina-Hernandez, et al., Scientific Reports, 7, 17645 (2017).